

Doctoral Dissertation

**Light Transport Acquisition via
Selective Light Path Measurement**

Takafumi Iwaguchi

February 20, 2019

Graduate School of Information Science
Nara Institute of Science and Technology

A Doctoral Dissertation
submitted to Graduate School of Information Science,
Nara Institute of Science and Technology
in partial fulfillment of the requirements for the degree of
Doctor of ENGINEERING

Takafumi Iwaguchi

Thesis Committee:

Professor Yasuhiro Mukaigawa	(Supervisor)
Professor Yoshinobu Sato	(Co-supervisor)
Associate Professor Takuya Funatomi	(Co-supervisor)
Assistant Professor Hiroyuki Kubo	(Co-supervisor)
Assistant Professor Kenichiro Tanaka	(Co-supervisor)

Light Transport Acquisition via Selective Light Path Measurement*

Takafumi Iwaguchi

Abstract

An active measurement, that senses the scene with a camera under controlled illumination, is one of the common techniques in computer vision field. Most of the conventional techniques rely on ideal light transport, or a response to the illumination of the scene. However, since an actual light transport depends on scene geometry and light behavior, undesired light transport such like inter-reflections and scattering could degrade the measurement. The goal of this thesis is to acquire desired light transport for further application such like to analyze the light behavior, to visualize the meaningful information, and to capture the appearance of objects in the real world, that are important tasks in the field of computer vision and computer graphics. To acquire the desired light transport, we focus on the light path from a light source to a sensor cell in the camera. In the conventional imaging, since the camera forms image by integrating all the light to sensor cells from various directions during exposure, the information of each path is lost. In order to acquire light transport before integration, we propose a selective path measurement. We control illumination and exposure to specify the path for the measurement. Our contribution also includes the proposal of the analysis and the application of the light transport. We tackle two problem settings. The first problem is an optical tomography of diffuse surface object that has a diffuse surface and a transparent body, like grapes. We propose acquisition of the light transport along straight paths inside the object. We propose a light path model and reconstruction algorithm. We demonstrate that our framework successfully

*Doctoral Dissertation, Graduate School of Information Science, Nara Institute of Science and Technology, February 20, 2019.

reconstructs the interior of a real object. The second problem is a light transport acquisition of projector-camera system. We propose novel acquisition according to the transport distance. We demonstrate our acquired light transport can be applied for various visualization and application.

Keywords:

light transport, light path model, optical tomography, projector camera system

Contents

1. Introduction	1
1.1 Background	1
1.2 Contributions	2
1.3 Structure of the Dissertation	5
2. Theory of light transport	6
2.1 Plenoptic function	6
2.2 Light transport and representation	6
3. Related work	9
3.1 Light transport acquisition for optical tomography	9
3.2 Light transport acquisition for the projector-camera system	10
4. Light transport acquisition of diffuse surface object	11
4.1 Introduction	11
4.2 Acquisition of light transport inside diffuse surface object	12
4.2.1 Distribution of the absorption coefficient and total absorption	12
4.2.2 Radon transform	12
4.2.3 Shortest path model	13
4.2.4 Model validity in the real situation	15
4.2.5 Setup of the measurement	16
4.2.6 Light path alignment	17
4.2.7 Observation rate of the light path	19
4.3 Reconstruction	22
4.3.1 Formulation as an optimization problem	23
4.4 Experiment	27
4.4.1 Appropriate setup of the measurement	27
4.4.2 Experiment on a real object	30
4.4.3 Measurement of arbitrary convex shape	33
4.4.4 Effect of scattering	33
4.5 Conclusion	36

5. Light transport acquisition of projector camera system	37
5.1 Introduction	37
5.1.1 Distance of light transport	37
5.1.2 Light transport in projector camera system	39
5.1.3 Our contribution	39
5.2 Acquisition of plane-to-ray light transport	41
5.2.1 Epipolar geometry and light transport	41
5.2.2 Light Multiplexing using Delay and Exposure	43
5.2.3 Delay-Exposure Image Stacks	46
5.2.4 Efficiency of light transport acquisition for limited range	48
5.3 Acquisition of full light transport	48
5.3.1 Illumination multiplexing	49
5.3.2 Hardware	52
5.4 Experiments	52
5.4.1 Analysis of light behavior	52
5.4.2 Relighting	55
5.4.3 Improving SNR by Multiplexing	56
5.4.4 Efficient Acquisition of Short Range Transport	58
5.4.5 Sharpening epipolar imaging	60
5.4.6 Epipolar direct/global separation	62
5.4.7 Visualization of vein	64
5.4.8 Appearance capture for graphics	64
5.4.9 Material Recognition of Subsurface Scattering	67
5.4.10 Acquired materials	69
5.5 Conclusion	72
6. Conclusions and Future work	73
6.1 Conclusions	73
6.2 Future work	74
Acknowledgements	75
References	76
List of Publications	85

List of Figures

1	Illustration of light transport	2
2	Undesired light transport.	3
3	Schematic illustration of selective path measurement.	4
4	Definition of target light transport.	5
5	Ray representation in 3D space.	7
6	Example of diffuse surface object.	12
7	Relation between the path and sinogram coordinates.	13
8	Transmission of rays when parallel rays are cast.	14
9	Observation of an egg.	14
10	Illustration of an egg observation.	15
11	Shortest-path model.	15
12	Applicable and non-applicable material of our model.	16
13	Setup of the measurement.	17
14	Missing area of sinogram according to θ_l	19
15	A missing area of sinogram.	21
16	Coverage of the measurement vs θ_l	22
17	Rays passing thorough a cell of the distribution.	25
18	Sinogram and reconstructed interior by FBP and proposed method according to setup.	28
19	Optical setup for the real world experiment.	29
20	Acquired sinogram.	31
21	Reconstructed interior.	32
22	Measurement of the object with triangle shape.	33
23	Illustration of the rendered scene.	34
24	Top views and projections for different types of scattering.	35
25	Sinogram and reconstruction for different scattering coefficients.	35
26	Light transport distance in the scene.	38
27	Corresponding illumination for the same transport distance at dif- ferent points.	38
28	Full light Transport between projector and camera.	39
29	Plane-to-ray Light Transport.	42
30	Indirect image captured with various delay and exposure.	42

31	Timing diagram of projector illumination and camera rolling shutter for epipolar imaging.	45
32	An image stack.	47
33	Light transport matrix and the order of the acquisition.	49
34	Illustration of full light transport acquisition.	50
35	Full Light Transport is defined as transport an illuminated pixel to a sensor pixel.	50
36	Illustration of illumination function.	51
37	Prototype.	52
38	Delay sweep profiles of various kinds of light behavior.	54
39	Two dimensional profiles for various kinds of light behavior.	55
40	Relighting under virtual single line illumination.	55
41	Relighting under virtual checkerboard pattern illuminations from full light transport.	57
42	Effect of illumination multiplexing for relighting with virtual single line.	58
43	Effect of illumination multiplexing for relighting with virtual patterns.	59
44	Scene with wide range of light transport.	61
45	Appearance according to Delay Range.	61
46	Light Transport Matrix.	62
47	Sharpening epipolar imaging.	63
48	Comparison of direct/global separation.	65
49	Visualization of vein.	66
50	Appearance capture for graphics.	68
51	Material classification using plane-to-ray light transport.	70
52	Confusion matrix of material classification.	71
53	Appearance and profiles of various materials.	71

List of Tables

1	RSME and Max of Absolute Error versus the light angle.	29
---	--	----

1. Introduction

1.1 Background

An active measurement, that senses the scene with a camera under controlled illumination, is one of the common techniques in computer vision field, such like the active stereo [1, 2], as in the photometric stereo [3, 4], and imaging radar [5]. The conventional active measurement techniques computes results from captured images. Light transport is a key factor of the active measurement. Illustration of light transport is shown in Fig. 1. Let us consider a case that we perform the active measurement of the scene. Multiple light sources and multiple photo-detectors (camera sensor can be regarded as an array of photo-detectors) are used for the measurement. Light evolves after it starts from a light source, interacts with the scene, and then finally is observed by photo-detectors. Light transport is a response of the scene to the incident light that describes a relationship between the incident light and the outgoing light.

The acquisition of light transport is important task in the fields of both computer vision and computer graphics for its application. The light transport itself is a great clue for understanding light behaviors such like diffuse reflections, diffuse and specular inter-reflections, and subsurface scattering in the scene. In active measurement, the result, (depth or normal) is computed from the light transport. Light transport is also applied for image-based relighting that allows us to synthesize an image of the scene relighted with the arbitrary illumination. A goal of this thesis is to acquire the light transport for further applications.

The light transport is complicated process relating to optical phenomenon and scene geometry. This makes its acquisition and analysis difficult. We describe this problem by taking Fig. 2 for an example. The most of the conventional techniques rely on the ideal measurement. For example, the active stereo techniques assume diffuse reflection on the surface from the direct illumination. Since inter-reflection between multiple objects (in the yellow line) is not following the assumption, it cause the wrong estimation. Also, the scattering in translucent material (in the orange line) degrades the estimation since it exhibit different response to the illumination. To deal with these problems, the patterns that is prone to inter-reflection have been proposed [6], or polarization has been utilized for descattering

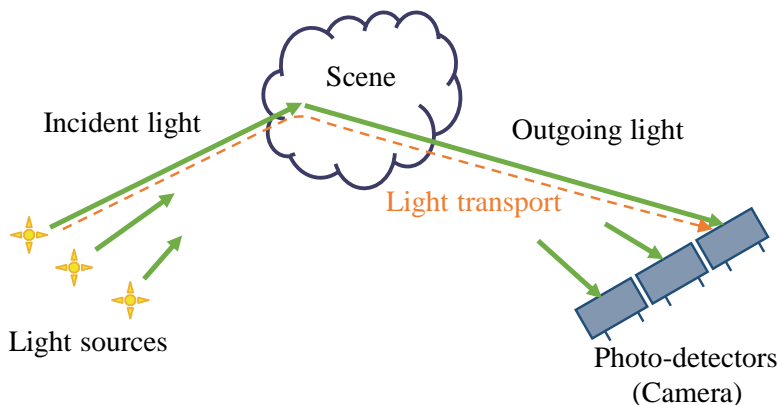


Figure 1. Illustration of light transport. Light transport describes the relationship between incident and outgoing light.

[7, 8, 9], however, they have disadvantages that the former only deals with long-range inter-reflection, and latter tends to be suffered from bad signal-to-noise ratio. Moreover, the desired light transport is different for its purpose. The acquisition of desired light transport is always an open problem.

Another problem is how to utilize the acquired light transport for analysis and application. Since the acquired light transport and its analysis are closely related, the analysis specific to the light transport is required.

1.2 Contributions

For acquisition of the desired light transport, we focus on a light path of the light transport. Let us review Fig. 2. Light paths of the light transport are shown in green, yellow, and orange lines. While all the paths connect the illumination and the camera, they are different due to the interaction with the scene. This implies that we can acquire light transport separately if we measure the light along each path selectively.

In this thesis, we propose a **light transport acquisition by measuring light paths selectively** so that we filter desired paths from all the paths involve; we can analyze the specific behavior of the light, and take away undesired paths. The methodology of the light transport acquisition depends on the target object and the characteristic of desired paths. We specify paths by considering the

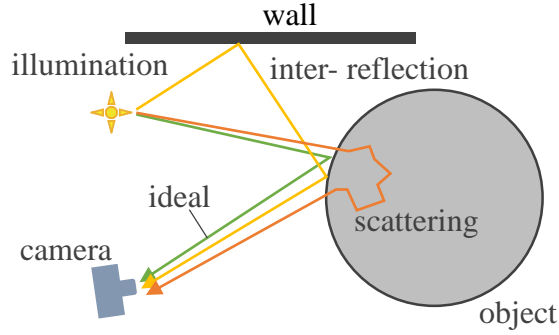


Figure 2. Beside ideal light transport (green), there is undesired light transport caused by inter-reflections (yellow), or scattering (orange).

geometry and the measurement setup, and selectively acquire the light transport along the path.

In order to describe our concept, we compare our method with the conventional imaging by a camera as shown in Fig. 3 (a). Since light from multiple light sources interact with the scene differently, the light travel through different paths in green, yellow, and orange, and received by the same sensor cell. In the camera, image is formed by integrating all the light to sensor cells from various directions during exposure. This means the original information of received light through each path, such as direction and change of radiation is lost. Therefore, the light transport along each path is not recovered from the images. In the presence of inter-reflection and scattering, the active measurement using conventional imaging fails. In selective path measurement, we specify each path by controlling illumination and exposure as illustrated in Fig. 3 (b). The sensor cell only receives the light from ideal path (green), the desired light transport is acquired.

We tackle two problem setting in this thesis; (1) an optical tomography of the diffuse surface object and (2) the light transport acquisition in projector-camera system.

Both types of light transport are illustrated in Fig. 4. A major difference of two types of light transport is a coordinate system that define the light transport.

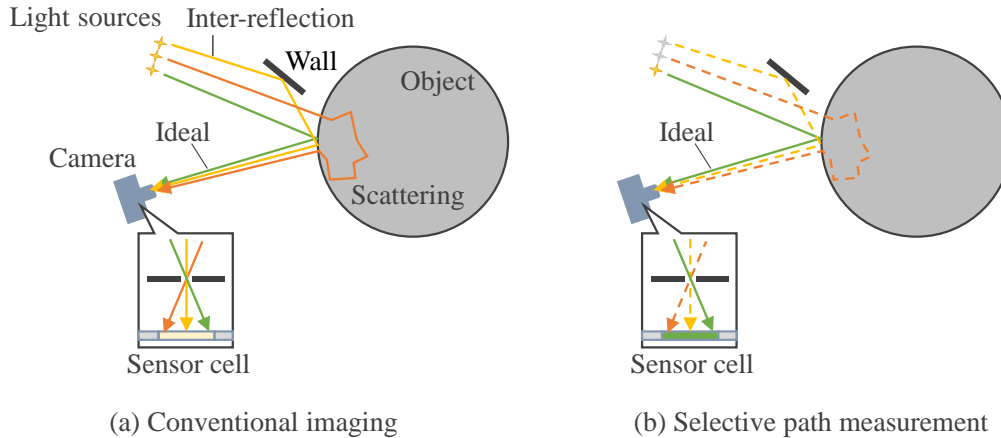


Figure 3. Schematic illustration of selective path measurement. In conventional imaging (a), different light paths can reach a single sensor cell that output a single value. We measure a radiance of light through a specific path (b) in our framework.

In (1), light transport is defined by the incident and outgoing points, which are defined on the object’s surface as shown in Fig. 4(a). This definition is appropriate for analyze the light transport in the single object, regardless of the measurement setup. Our target is called a diffuse surface object who has diffuse surface and transparent body. We propose a novel acquisition specialized for the diffuse surface object. In (2), the light transport is defined in a measurement setup as shown in Fig. 4(b). This definition is appropriate for analyze the light transport in the scene with multiple objects. It is still usable to analyze the light transport in the object, however, the geometric relationship must be considered. We acquire two different types of the light transport, called plane-to-ray light transport and full light transport, respectively. The acquisitions is made according to the light transport distance by utilizing a novel synchronized projector camera system.

Another contribution of this thesis is **the proposal of the analysis and the application of the light transport**. In (1), the interior of the object is reconstructed from the light transport. To reconstruct the interior, we propose a light path model inside the object and the reconstruction algorithm. In (2), we show various application of plane-to-ray and full light transport. We show the light transport allows us to visualize and to analyze in efficient way.

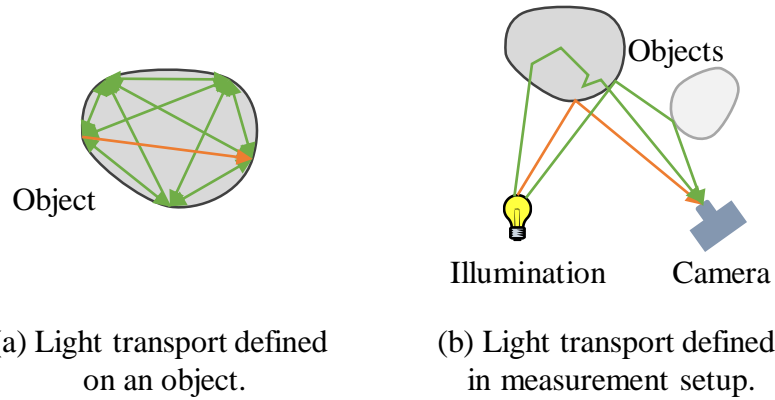


Figure 4. Definition of our target light transport. We focus on light transport in the objects in (a) and light transport in a measurement setup in (b).

1.3 Structure of the Dissertation

This thesis is organized as follows. Chapter 3 presents the related work to show our contribution. It includes the acquisition of the various kind of light transport. It also includes the conventional approach to related applications. Chapter 4 describes the optical tomography of the diffuse surface object. We describe the measurement, the path model, and the reconstruction of the interior. Chapter 5 describes the light transport acquisition of projector-camera system. We describe the measurement and show applications of the acquired light transport. Chapter 6 concludes this thesis with future work.

2. Theory of light transport

2.1 Plenoptic function

Before considering about the light transport, let us consider about the description of the light. The plenoptic function [10] is introduced by Adelson and Bergen to describe all the light in the scene. We define the radiance of the light ray travelling in the 3D space by 7D plenoptic function

$$P(x, y, z, \theta, \phi, \lambda, t), \quad (1)$$

where (x, y, z) is the 3D location, (θ, ϕ) is the direction as shown in Fig. 5, λ is wavelength, and t is time. The plenoptic function contains all the information construct any image of the scene at any time. Image-based rendering [11, 12] is one of the application of the plenoptic function.

The measurement of the plenoptic function is not a trivial task due to its large sampling space [13]. In most applications, all the dimensions are not necessary. The light field [14, 15] is a 4D slice of the plenoptic function. The light field has been an interest of many studies since the light field can be applied for view interpolation, confocal imaging [16] and refocusing [17, 18], alongside its acquisition techniques.

2.2 Light transport and representation

The light transport is a response of the scene to the active illumination. We have defined the light transport as a response to the incident light of the scene, in other words, it is a relationship between the incident and the outgoing light. Therefore, the light transport can be regarded as a function of incident and outgoing rays. By using plenoptic functions of incident light $P_{incident}$ and outgoing light $P_{outgoing}$, such as $f(P_{incident}, P_{outgoing})$. However, this expression could have up to 14 parameters and is very redundant considering possible variation in the scene.

Now we discuss about the representation of the light transport in an object. The light transport in an single object have been researched for long decades. In the context of computer graphics, the light transport is described with re-

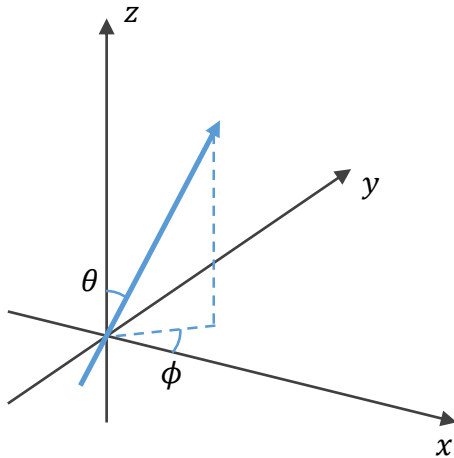


Figure 5. Ray representation in 3D space.

duced parameters in order to render the realistic appearance with limited representation of the data and the limited sampling cost. Bidirectional Scattering Surface Reflectance Distribution Function (BSSRDF) [19], Spatially-varying Bidirectional Reflectance Distribution Function (SVBRDF) [19] and Bidirectional Texture Function (BTF) [20] are examples of general representation of light transport. While some works tackle with acquisition of high dimensional transport like SVBRDF [21, 22, 23, 24] and BTF [20], the some works have propose more compact representation and acquisition like reflectance field [25] by the light stage, incident light field [26], and surface light fields [27]. One of the most popular compact representations is BRDF. Many BRDF models are proposed for realistic synthetic images by considering the surface property like diffuse reflection [28], glossy reflection [29] and normal variation[30]. Many techniques of the acquisition of isotropic BRDF are proposed [31, 32, 33] and some of them provides the database for the materials. In the contrast of BRDF, BSSRDF is difficult to model without assumption due to its high dimensionality. To deal with this problem, some work [34, 35, 36] assume a homogeneous medium. In Sec. 4, we consider the light transport defined on an object that is specialized for tomographic reconstruction.

Next, we consider about the representation of the light transport in a measurement system. The measurement system consists of multiple light sources and multiple photo-detectors. In this case light transport can be defined as a received

light of photo-detectors when a specific light source is turned on. Let vector \mathbf{p} denotes a state of light sources and vector \mathbf{c} denotes intensities of photo-detectors. A relationship between two vectors are written as

$$\mathbf{c} = \mathbf{T}\mathbf{p}, \tag{2}$$

where \mathbf{T} is a light transport matrix. This representation is applied for the projector camera system, since the projector can be regarded as multiple illuminations and the camera as multiple photo-detectors. By considering spatial relationship of projector and camera pixels, it is also described in four dimensional function since it is a relationship between incident light represented in 2D projector pixels and outgoing light represented in 2D sensor pixels. In Sec. 5, we define novel light transport by considering spatial relationship of projector pixels and camera pixels.

3. Related work

3.1 Light transport acquisition for optical tomography

In chapter 4, we tackle with the diffuse surface object where its surface exhibit diffusion and its medium exhibit only absorption. Optical tomography [37] is a technique to inspect an object by light radiation and the measurement from outside. The optical tomography reconstruct the distribution inside of the object based on the interaction between the medium of the object and the light. The interaction such like absorption and scattering occurs everywhere in the medium, however, what we measure is the light transport.

We define reconstruction as the process to estimate interior from the measurement. In the tomography, the distribution and light transport must be transformed into one another. The method of light transport acquisition must be designed by considering the reconstruction.

Optical projection tomography (OPT) [38] is a simple technique that is the same as X-ray computed tomography (CT) except that it uses visible or infrared light instead of X-rays. It is assumed that light travels in a straight direction in the object, as for X-rays. This assumption allows us to reconstruct the interior by Radon transform [39] that gives the relationship between the measurement and the interior. OPT provides a clear three-dimensional reconstruction of a small specimen and has contributed to many biological studies; however, it cannot deal with a diffuse surface.

For the object exhibit scattering, Radon transform is no longer applicable. Techniques have been proposed to cope with scattering; e.g., techniques for single scattering [40] and multiple scattering [41, 42, 43]. Scattering in the human body is approximated as an isotropic diffusion in diffuse optical tomography; applications of the approximation are mammography [44] and functional imaging of the brain [45, 46].

Our contribution is to propose a light transport model for the diffuse surface object and to propose a light transport acquisition and reconstruction method based on the model.

3.2 Light transport acquisition for the projector-camera system

In chapter 5, we acquire the light transport between projector and camera. The difficulty of sampling light transport in projector-camera system is its sampling space due to the high resolution of today’s devices. The efforts have been made to represent light transport compactly and to acquire it efficiently. In dual-photography, Sens et al. [47] takes a hierarchical approach by assuming short-range transport. A sparseness of light transport matrix is assumed in [48, 49] for compressive sensing and symmetry is assumed in [50]. Under the assumption of low-rank, the matrix is reconstructed by kernel Nystrom method [51] and eigenvectors are measured directly by optical computing [52].

In this work, we acquire light transport matrix without the assumption of neither sparsity nor low-rank. Our method allows us to acquire light transport according to its transport distance. If the range of the transport distance is limited, the number of sampling could be reduced.

4. Light transport acquisition of diffuse surface object

4.1 Introduction

The measurement of an object’s interior is important in various applications, such as the detection of foreign objects in food and the inspection of the human body in a medical examination. An optical measurement is a safe inspection technology that does not use X-rays and has no risk posed by a radiation dose. Furthermore, optical measurement provides functional information on optical properties; e.g., blood flow is estimated from spectral absorption. One of the challenging problem of optical measurement is optical tomography. Like X-ray Computed Tomography (CT), optical tomography measures an 3-dimensional internal structure or interior of objects using optics.

In the tomography, the interior is estimated from the transport measured by sensors surrounding the object, rather than is measured directly. There are two requirements to reconstruct the distribution from the transport. First, the path model of the transport is required to transform the measured transport into the distribution. Second, a measurement technique is required so that the transport along the specific path considered in the model is measured.

We aim to acquire light transport according to a path model so that the interior is reconstructed from the acquired light transport. We target objects that has a diffuse surface and an interior that is assumed transparent, where light is absorbed but not scattered. Fruits like grapes (Fig. 6), light bulbs with white glass, and hollow plastic bottles are examples of such objects.

In this section, we propose a *shortest path model* that assume the light travels shortest distance in the diffuse surface object as a light path model in the diffuse surface object. We propose selective path measurement for light transport acquisition according to the model. We also propose a reconstruction method of interior from acquired light transport. Our contribution also includes coverage analysis of measurement and a design of measurement setup.



Figure 6. Example of diffuse surface object. A grape has a diffuse surface and a transparent body.

4.2 Acquisition of light transport inside diffuse surface object

4.2.1 Distribution of the absorption coefficient and total absorption

We reconstruct a distribution of the absorption coefficient σ of the target's interior. The absorption coefficient represents how much light is absorbed as light travels a unit distance. We now define the total absorption A by following Lambert-Beer law, as the logarithm of I_o (the intensity of light after light travels through the target) divided by I_i (the intensity of light before entering the target):

$$A = \log I_o - \log I_i. \quad (3)$$

4.2.2 Radon transform

The relationship between the total absorption and absorption coefficient is described by the *Radon transform*. For a simplicity, we consider the problem in two dimensions. When a ray propagates through an area Ω , the total absorption is an integral of the absorption coefficient along the path:

$$A_\Omega = \iint_{x,y \in \Omega} \sigma(x,y) dx dy. \quad (4)$$

The path of a ray is generally assumed straight in the Radon transform. Let us describe a straight ray in polar coordinates fixed on the object as illustrated in

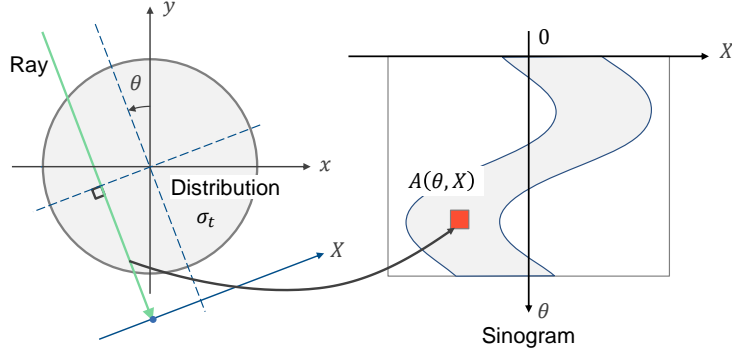


Figure 7. Relation between the path and sinogram coordinates. Total attenuation along a ray is stored in a specific coordinate in sinogram.

Fig. 7. A radon transform about a ray (X, θ) is written as

$$A(\theta, X) = \int_{-\infty}^{\infty} \sigma(z \sin \theta + X \cos \theta, -z \cos \theta + X \sin \theta) dz. \quad (5)$$

We reconstruct a distribution of the absorption coefficient using the inverse Radon transform that is derived from Eq. (5). The reconstruction of the interior requires the total absorption of rays passing through the interior (i.e., $A(\theta, X)$) for all possible θ and X . Ideally, these rays are acquired by measuring the transmitted rays when parallel rays are cast toward the target from various angles. This method works well when the paths of rays are not disturbed by the target as in the case of X-rays. However, as illustrated in Fig. 8, each ray entering the object spreads when the target has a diffuse surface. The transmitted rays are no longer parallel and it is difficult to determine paths of the measured rays.

4.2.3 Shortest path model

We model light paths in a diffuse surface object as a first step to determining the paths of rays. We discuss about the light path model by taking an egg in Fig. 9 as an example. A egg consists of a shell, white and yolk. In order to inspect the egg, we illuminate the shell with a LED pointer. When the shell is illuminated from a right side, a silhouette of yolk appears on a left side as shown in Fig. 9(b).

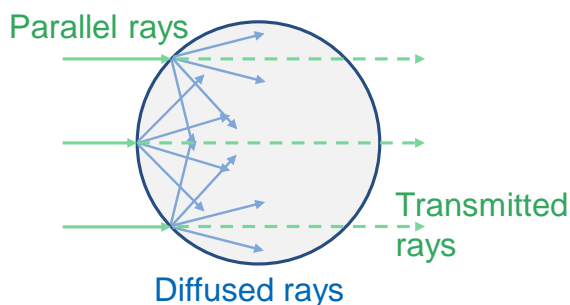


Figure 8. When parallel rays are cast, they spread at the incident points on the surface.

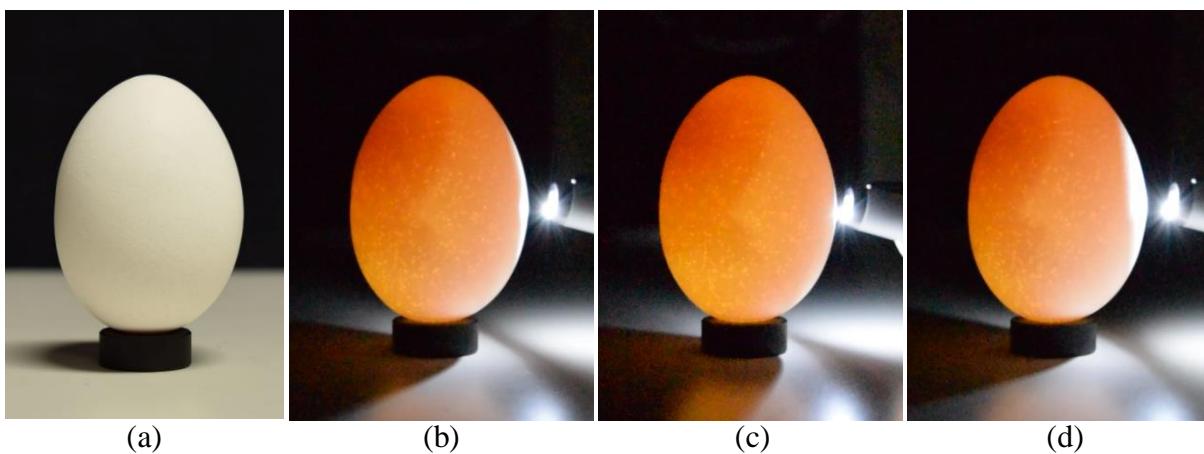


Figure 9. Observation of an egg using LED pointer. The silhouette of yolk appears on the opposite side of illuminated point.

And the silhouette moves corresponding to the moving illumination as shown in Fig. 9(b), (c) and (d). We consider how the silhouette appears by using an illustration of this observation (Fig. 10). When light ray from the pointer hit surface of the shell, it should diffuse and should form spreading paths from the incident point. These paths are mostly straight, since the white should be weak scattering media. Then rays travel through yolk should be attenuated and the others should not, as a result they make such a silhouette.

We generalize this observation as a model. In this model, we assume light diffuse at the incident point and travel straight through medium. Therefore,

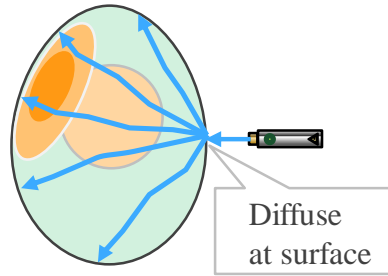


Figure 10. Illustration of an egg observation. Spread rays at surface make the silhouette.

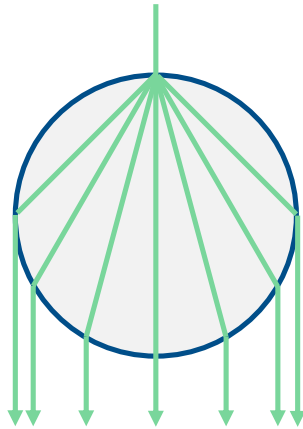


Figure 11. In shortest-path model, the rays are modelled as straight in the body after diffusion on the incident point.

paths in the object are regarded as a set of straight rays spreading from the incident point as illustrated in Fig. 11. Since the straight path inside the object travels shortest distance in the object, the model is called *shortest path model*.

4.2.4 Model validity in the real situation

In the real situation, the paths in the object do not always follow the shortest-path. The path in the real situation is illustrated in Fig. 12. One of the difficult targets could be the object with thick skin. Because the incident point of the path is determined as a first point where the light from the source hit the surface. An actual incident point of the path should lie on the inner boundary between

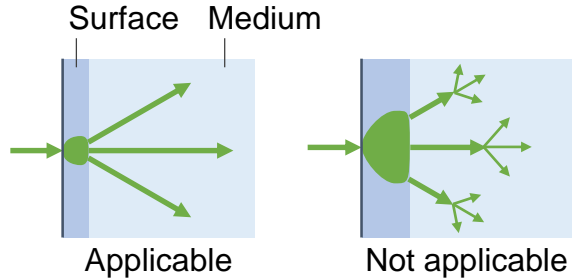


Figure 12. Applicable and non-applicable material of our model. We assume diffusion happens at the exact incident point on the surface, and there is no scattering.

the skin and the body, therefore these two points do not match when the skin is thick and the light is spread by the diffusion in the skin. Our model is applicable when the skin is thin enough.

Another factor that could affect the reconstruction is the scattering in the medium. When the scattering occurs, the path in the medium is no longer straight. The effect of the scattering is evaluated in Sec. 4.4.4.

4.2.5 Setup of the measurement

Because the light path is modeled as a straight line, a path in the object is uniquely determined if both ends of the path are specified. If there is light in a large area, which means many rays are cast as illustrated in Fig. 8, the exact point that a ray enters is difficult to determine. Incident light should fall in a small area to avoid this problem. Meanwhile, rays exiting the object are measured by shooting the surface of the target. The shooting is repeated while the object is rotated to collect rays entering at and exiting from various points. Accordingly, a setup will consist of a narrow light source, camera, and rotary stage on which the target is placed, as shown in Fig. 13.

We assume the orthogonal projection or perspective projection as the projection model of the camera. In the case of orthogonal projection, point of incident and outgoing ray are determined with regardless to the placement of the object and camera. Meanwhile, it requires a special optics like telecentric lens, moreover, it cannot handle with the objects bigger than the size of the lens. In the

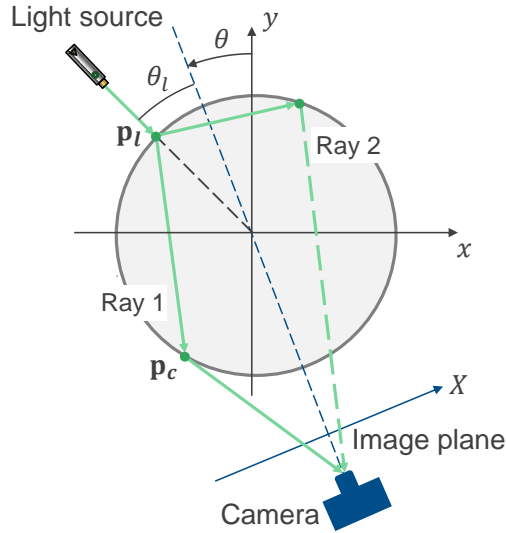


Figure 13. Setup of the measurement. Light source and camera are pointing to the center of rotation.

case of the perspective projection, while the placement of the object and camera must be taken into account, lens is off-the-shelf and it is easier to measure big object thanks to the wide Field of View (FOV).

4.2.6 Light path alignment

A raw measurement must be converted into light transport to reconstruct interior. We call this conversion *light path alignment*. Geometry of light path and change of intensity are considered in light path alignment.

First, we discuss about the geometry of light path. Paths of a ray in a three-dimensional scene should be computed because they are required for the reconstruction. The three-dimensional coordinates of the points at which a ray enters and exits are determined as follows. The point at which a ray enters is determined by calculating the intersection of the ray from the light source and a contour of the target. Similarly, the point at which a ray exits is determined by calculating the intersection of the ray from the camera and a contour of the target. To uniquely determine these intersections of the ray and the contour of the target, all the contours of the target must not be occluded from the light source or the camera. Therefore, the shape of the object need to be convex in our measure-

ment. To obtain a target contour, we compute a visual hull [53] as the shape of the target in the following steps. In order to capture the silhouette of the target, we place the diffuse plane behind the target from the camera view and illuminate the plane so that it looks evenly illuminated. A silhouette is then extracted by binarization after subtracting the background from the captured image. A visual hull is finally computed by taking an intersection of the perspective projection of the silhouette on the object space. Since our measurement needs the shape of the target to be convex, it is reasonable to utilize a visual hull that is only applicable for convex shapes.

The geometry of light paths also affects the intensity of rays. A intensity distribution through the surface is described by the bidirectional transmission distribution function (BTDF) $f_T(\omega_i, \omega_o)$, where ω_i is the incidence angle and ω_o is the outgoing angle of the light. For accurate reconstruction, the effect at the surface must be compensated. To compensate this effect, $f_T(\omega_i, \omega_o)$ within sampling range must be measured additionally. A intensity of light transport inside the object is computed by cancelling BTDF. Also, refraction at the surface also affects the intensity where the effect is governed by Fresnel equation. We assume this effect is included in BTDF.

After light path alignment, we can employ a sinogram for the representation of acquired rays. We consider polar coordinates (X, θ) fixed on the target. The origin is at the center of rotation in the measurement setup. In a 2D representation of sinogram, horizontal and vertical axes respectively correspond to (X, θ) , and an attenuation of the ray is stored.

For each ray, we define an intersection of the ray and a contour of the object in Cartesian coordinates (x, y) that share the same origin as the polar coordinates (X, θ) . By denoting the intersection of a ray from the camera and a target by \mathbf{p}_l and the intersection of a ray from the camera and a contour by \mathbf{p}_c , the angle of a path θ is calculated as

$$\theta = \arg(\mathbf{p}_l - \mathbf{p}_c), \quad (6)$$

where $\arg(\cdot)$ denotes the angle between a vector and the x -axis. A displacement of path X is calculated according to

$$X = \mathbf{p}_l^\top \cdot \begin{bmatrix} \sin \theta \\ \cos \theta \end{bmatrix}. \quad (7)$$

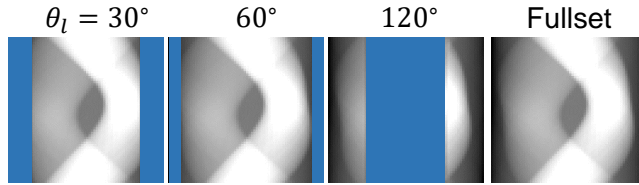


Figure 14. Missing area of sinogram according to θ_l . While sides of sinogram are missing at $\theta_l = 30^\circ, 60^\circ$, central part is missing at 120° .

4.2.7 Observation rate of the light path

When the surface of the object is measured using a single camera, not all rays in the object are measured depending on the object’s shape and the optical setup. We now look at Fig. 13 to understand the unobserved rays. Rays 1 and 2 cast from the light source enter the object at the same point but exit from different points, before being measured by the camera on the opposite side of the object. While ray 1 is observable because it reaches the surface visible from the camera, ray 2 is unobservable because it reaches the surface unobservable from the camera.

Let us assess the effect of unobserved rays. We simulate the measurement for the case where the camera model is perspective and the target is a cylinder and generate sinograms for different θ_l in Fig. 13. Figure 14 shows generated sinograms and the “fullset” sinogram that contains sufficient rays with which to reconstruct the full interior. There are missing areas in the sinograms owing to the unobserved rays. In the case of $\theta_l = 30^\circ$, there are missing areas on both the sides of the sinogram. Likewise, in the case of $\theta_l = 60^\circ$, there are missing areas on the sides but the areas are smaller. In contrast, a missing area appears at the center in the case of $\theta_l = 120^\circ$.

We next evaluate the observation rate of rays. Here we measure the observation rate using coverage—a ratio of missing area to the area of sinogram. To describe the missing part, we use the distances d_{\min} and d_{\max} as shown in Fig. 15. From the definition of d_{\min}, d_{\max} , the coverage is given by $d_{\max} - d_{\min}$.

Case of orthogonal projection

d_{\min}, d_{\max} are calculated as follows: for the case of $0 \leq \theta_l \leq \frac{\pi}{2}$,

$$d_{\min} = 0 \quad (8)$$

$$d_{\max} = \cos\left(\frac{\pi}{4} - \frac{\theta_l}{2}\right), \quad (9)$$

and for the case of $\frac{\pi}{2} \leq \theta_l \leq \pi$,

$$d_{\min} = \sin\left(\frac{\theta_l}{2} - \frac{\pi}{4}\right) \quad (10)$$

$$d_{\max} = 1. \quad (11)$$

The coverage takes its maximum at

$$\theta_l = \frac{\pi}{2}. \quad (12)$$

Case of perspective projection

Let θ_{FOV} denotes FOV. d_{\min}, d_{\max} are calculated as follows: for the case of $0 \leq \theta_l \leq \frac{\pi - \theta_{FOV}}{2}$,

$$d_{\min} = 0 \quad (13)$$

$$d_{\max} = \cos\left(\frac{\pi}{4} - \frac{\theta_l}{2} + \frac{\theta_{FOV}}{4}\right), \quad (14)$$

for the case of $\frac{\pi - \theta_{FOV}}{2} < \theta_l \leq \frac{\pi + \theta_{FOV}}{2}$,

$$d_{\min} = \cos\left(\frac{3\pi}{4} - \frac{\theta_l}{2} - \frac{\theta_{FOV}}{4}\right) \quad (15)$$

$$d_{\max} = \cos\left(\frac{\pi}{4} - \frac{\theta_l}{2} + \frac{\theta_{FOV}}{4}\right), \quad (16)$$

and for the case of $\frac{\pi + \theta_{FOV}}{2} < \theta_l \leq \pi$,

$$d_{\min} = \cos\left(\frac{3\pi}{4} - \frac{\theta_l}{2} - \frac{\theta_{FOV}}{4}\right) \quad (17)$$

$$d_{\max} = 1. \quad (18)$$

The coverage takes its maximum at

$$\theta_l = \frac{\pi - \theta_{FOV}}{2}. \quad (19)$$

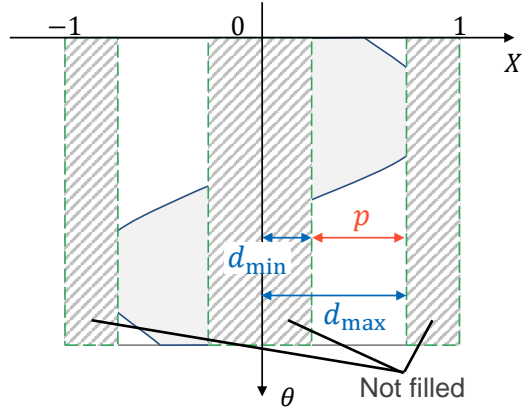


Figure 15. A missing area of sinogram. Coverage p is defined by the difference of d_{max} and d_{min} .

Fig. 16 shows the relationship between the coverage and θ_l for the perspective projection when the FOV is 30° and 60° . It is found that the coverage of FOV = 60° is lower than that of FOV = 30° for any θ_l . In addition, we show coverage in the cases of the orthogonal projection that were considered in a previous paper [54]. In the case of orthogonal projection, the coverage is satisfied at $\theta_l = 90^\circ$; hence, a lack of observations can be avoided using this angle. In contrast, the coverage is never satisfied in the case of perspective projection. The problem of insufficient observations is inevitable unless a single perspective camera is used.

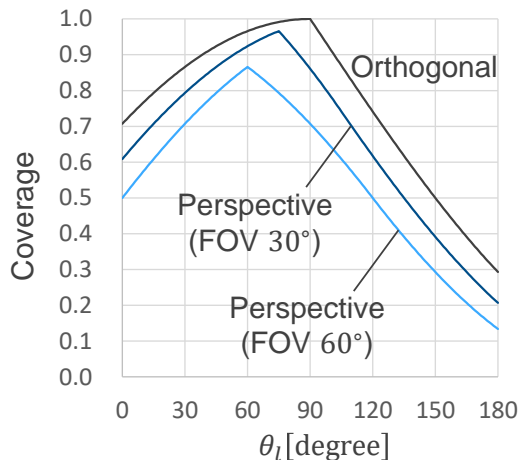


Figure 16. Coverage of the measurement vs θ_l . While coverage can be full at a specific θ_l for orthogonal projection, it is never satisfied for perspective projection.

4.3 Reconstruction

When there are insufficient observations, a possible solution is to modify the setup by adding another light source or camera to complete the observation. When it is possible to observe all the paths, the interior should be reconstructed most accurately. One of the difficulties of this approach is that an additional light source or camera must be precisely aligned because the reconstruction is sensitive to misalignment. Another difficulty is that the number and the placement of the light source and the camera depend on the shape of the object. Although the optimal configuration is difficult to find, it is not usable for other objects. Moreover, there is no guarantee of the existence of the configuration that makes the observation complete.

In this paper, we employ numerical optimization to deal with the problem of incomplete observations. The numerical optimization can be used with the multiple light sources and camera.

A reconstruction from insufficient observation have been actively studied for decades in field of medical imaging, since X-ray dose can be reduced by reducing radiation, however, it sometimes causes insufficient measurement. One of the problem is called short-scan. To reconstruct exact interior, the observation

requires a scan over certain angle, however, in short-scan problem, a scan angle is not sufficient. For this problem, reconstruction using back projection with a special filter has been proposed [55], however, it is known that the reconstructed interior is not exact [56]. A approach to such problem is iterative reconstruction that iteratively update the interior to minimize reprojection error. Algebraic Reconstruction Technique [57] and Simultaneous Algebraic Reconstruction Technique [58] has been used for improving reconstruction quality. To deal with missing angles, iterative methods based on filtered backprojection have been proposed [59, 60]. Our problem is different from short-scan problem, since the scan angle is sufficient.

Our problem is more similar to so called Region of Interest (ROI) reconstruction. In this problem, X-ray radiates only to a target region inside the body. As an analytical approach, methods based on Hilbert transform reconstruct an exact interior from the truncated projection data [61, 62]. However, they requires a measurement to include a specific boundary of the target, therefore, they cannot be applied in a straightforward way for our case. Moreover, our problem setting is different since we are trying to reconstruct whole region of the target.

In our problem, the exact reconstruction should not be possible since the observation is insufficient as we discuss in a next section. In recent years, numerical optimization has been studied to estimated a realistic interior with prior knowledge. They formulate optimization problem where prior is included as regularization term or constraint. Especially, convex optimization have been studied actively since regularization or constraints on the solution can be imposed in straightforward way. Some works took this advantage to reconstruct from small number of measurement by minimizing total variation [63], and compressive sensing [64]. We follow these approach to impose constraints that are designed for our problem.

4.3.1 Formulation as an optimization problem

In the case that the observations are insufficient, the correct reconstruction is difficult because there are multiple solutions that agree with the observation mathematically. We introduce two constraints to eliminate solutions that are not physically correct and to achieve convergence to a more realistic distribution.

The first constraint is the physical constraint (PC) on the range of the distribution of the absorption coefficient that is derived from the existing observations. This constraint rejects solutions that are physically wrong; however, there are still many possible distributions. The second constraint is regularization based on the total variation (TV) semi-norm that imposes smoothness on the distribution. This constraint allows convergence to a realistic solution by reducing the effect of noise of the observation.

We formulate the reconstruction as an optimization problem:.

$$\arg \min_{\boldsymbol{\sigma}} E(\boldsymbol{\sigma}) + \iota_C(\boldsymbol{\sigma}) + \lambda \|\boldsymbol{\sigma}\|_{TV}. \quad (20)$$

The first term is a data-fidelity term that implies that a reprojection of an estimated distribution by the Radon transform should be close to a sinogram $\mathbf{A}_{observed}$. The second term is the PC on the distribution and the third term represents TV semi-norm regularization. Because the objective function of Eq. (20) is convex, we employ the alternating direction method of multipliers to solve the problem.

Reprojection error of the Radon transform To derive the reprojection error, we rewrite the Radon transform (Eq. (5)) in matrix form. Let i denote an index of a cell of a discrete distribution after serialization. A Radon transform of a ray having index j is written as

$$A_j = \sum_i r_{ij} \sigma_i, \quad (21)$$

where

$$r_{ij} = \begin{cases} 1 & \text{(if ray } j \text{ hits } \sigma_i) \\ 0 & \text{(otherwise).} \end{cases} \quad (22)$$

By combining Eq. (21) for all rays as a linear system,

$$\mathbf{A} = \mathbf{R}\boldsymbol{\sigma} \quad (23)$$

is derived. In the optimization problem, reprojection error is computed by taking the difference between \mathbf{A} and the projection of estimated $\boldsymbol{\sigma}$ obtained using matrix \mathbf{R} . We consider reprojection error only for available observations and measure it using the $L - 2$ norm. Let $\mathbf{R}_{observed}$ denote the Radon transform for available

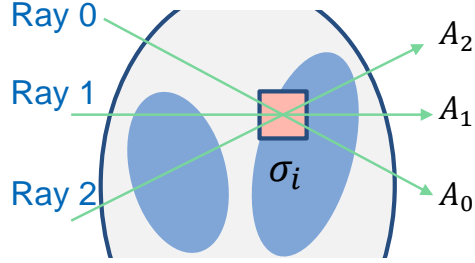


Figure 17. Rays passing thorough a cell of the distribution. Absorption of the cell must be smaller than the total absorption of all the rays.

observations and $\mathbf{A}_{observed}$ denote a sinogram of available observations. Finally, the data fidelity term is derived as

$$E(\boldsymbol{\sigma}) = \|\mathbf{A}_{observed} - \mathbf{R}_{observed}\boldsymbol{\sigma}\|_2^2. \quad (24)$$

Physical conditions of light absorption

The constraint is determined by the existing observations considering a physical condition of the coefficient of light absorbance. Because light does not increase in intensity as it travels through an object, the absorbance coefficient cannot be less than zero. The lower bound of the absorption coefficient σ_i is written as

$$\sigma_i \geq 0. \quad (25)$$

The upper bound of the absorbance coefficient can be determined by considering the relationship between the total absorption and the distribution of the absorbance coefficient. As Eq. (21) implies, the total absorption of a ray is the integral of the absorbance coefficient along the path. In the example presented in Fig. 17, only three light paths pass through σ_j . Therefore, σ_j must not exceed the total absorptions of the three light paths, and σ_j is thus constrained as $\sigma_j \leq \min(A_0, A_1, A_2)$. The absorption at a certain pixel must therefore not be higher than the minimum of all the projections that travel through the pixel. In the general case, the upper bound is written as

$$\sigma_j \leq \min_{i \in \chi_j}(A_i), \quad (26)$$

where χ_i is a set of rays that hit σ_j .

The lower and upper bounds form the box constraint of the solution. Let a set C denote the range of absorption:

$$C = [\mathbf{0}, \boldsymbol{\sigma}_{\max}], \quad (27)$$

where

$$\boldsymbol{\sigma}_{\max} = \left(\min_{i \in \chi_1}(A_i), \min_{i \in \chi_2}(A_i), \dots, \min_{i \in \chi_N}(A_i) \right)^\top. \quad (28)$$

The constraint is then represented by the indicator function $\iota_C(\sigma)$:

$$\iota_C(\boldsymbol{\sigma}) = \begin{cases} 0 & (\text{if } \boldsymbol{\sigma} \in C) \\ \infty & (\text{otherwise}). \end{cases} \quad (29)$$

Constraint about the spatial smoothness of the interior We define the TV norm $\|\cdot\|_{TV}$ as

$$\|\boldsymbol{\sigma}\|_{TV} := \sum_{i,j} \sqrt{|\nabla_1 \boldsymbol{\sigma}|^2 + |\nabla_2 \boldsymbol{\sigma}|^2}, \quad (30)$$

where ∇_1, ∇_2 are the discrete horizontal and vertical differential operators. The minimization of the norm forces the distribution to vary gradually while preserving the edges. This is preferable in most cases, and we can adjust the effect of the term by choosing a small λ whenever it is not suitable.

4.4 Experiment

4.4.1 Appropriate setup of the measurement

We determine the appropriate setup before performing an experiment in a real environment. We first investigate the characteristics of our reconstruction method based on the optimization by comparing with the conventional filtered back projection (FBP). Moreover, we compare the reconstructed interiors obtained under different setups of the measurement to evaluate the effect of the setup on the accuracy of the reconstruction. Synthetic sinograms are generated by solving the forward Radon transformation (Eq. (23)) for different θ_l . We also evaluate the interiors reconstructed by the FBP and our reconstruction method.

Fig. 18 shows the reconstructed interiors for $\theta_l = 0^\circ, 30^\circ, 60^\circ, 90^\circ,$ and 120° . In the cases of $\theta_l = 0^\circ, 30^\circ,$ and 60° , there are missing areas on both sides of the sinogram. The outer parts are not correctly estimated owing to the large missing areas at $\theta_l = 0^\circ$, but the central part is estimated correctly. There are similar tendencies in the results for $\theta_l = 30^\circ$ and 60° , but the errors are smaller because of the better observation.

It is found that our reconstruction method failed to reconstruct the center of the interior as for reconstruction by the FBP. This is because of the absence of observations of the center; no rays passing through the central area are observed, whereas more than one ray is observed in the previous cases. The whole interior needs to be reconstructed such that the center of the sinogram is not missing. In terms of quality, our method provides a better reconstruction than the FBP. Whereas the result of the FBP has line artifacts and blurring, a clear shape is reconstructed without artifacts using our method.

For quantitative evaluation, the Root Mean Squared Error(RSME) and the maximum of the absolute error are shown in Table 1. Note that the original distribution is varied in the range between 0 to 0.2. The RSME reflects the correctness of the reconstruction, which is discussed above. They are small at $\theta_l = 30^\circ$ and 60° , and increase as the number of failure pixels increases. The maximum of the absolute error reflects how the worst pixel is reconstructed. Referring to an absolute error in Fig. 18, the worst pixels are reconstructed from the missing area of the sinogram. It is confirmed that the absolute error is

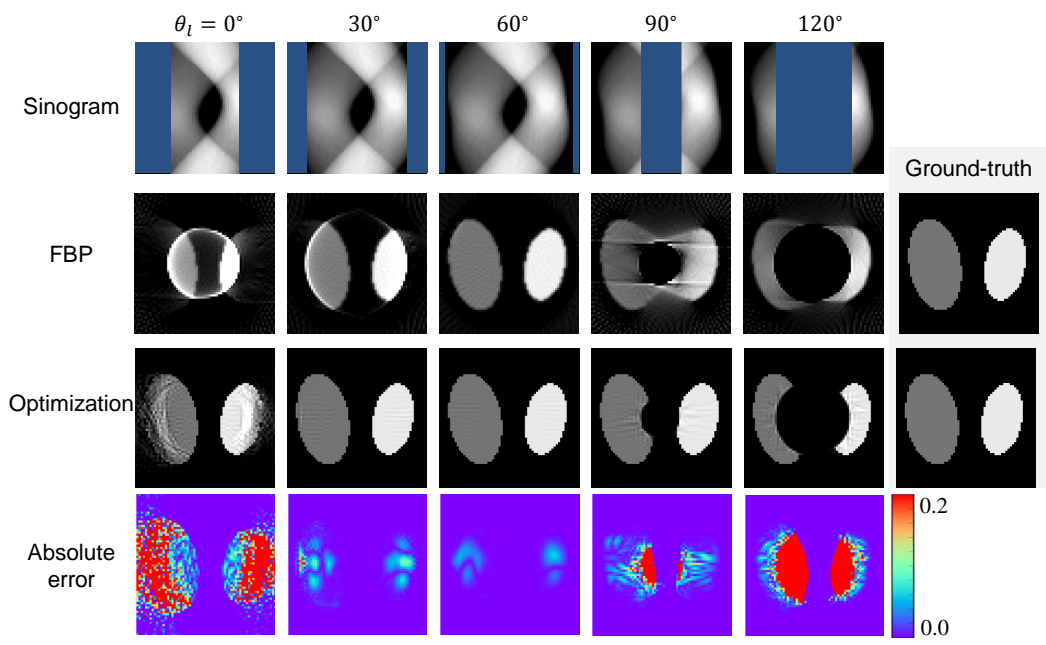


Figure 18. Sinogram and reconstructed interior by FBP and proposed method according to setup. When sides of sinogram are missing, optimization method reconstructs all the interior which FBP fails.

Light angle θ [°]	RSME	Max. of Absolute Error
0	3.15×10^{-3}	1.32×10^{-1}
30	2.57×10^{-4}	0.24×10^{-1}
60	1.32×10^{-4}	0.60×10^{-1}
90	2.31×10^{-3}	2.00×10^{-1}
120	7.55×10^{-3}	2.00×10^{-1}

Table 1. RSME and Max of Absolute Error versus the light angle. Small RSME reflects the correctness of the reconstruction, and the maximum of the absolute error reflects how the worst pixel is reconstructed.

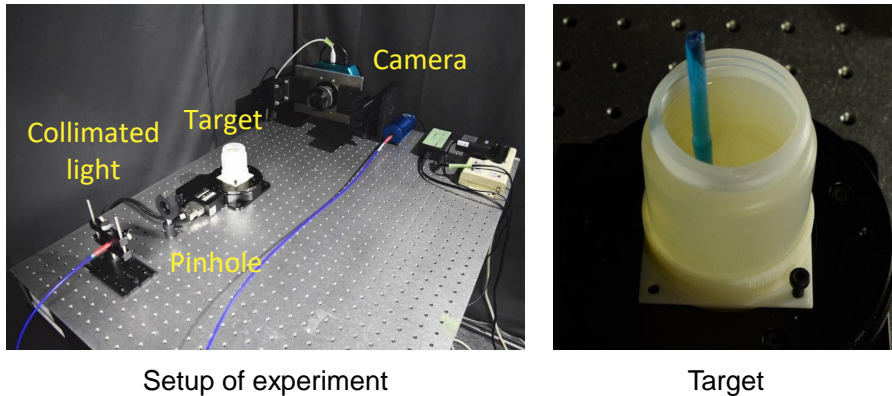


Figure 19. Optical setup for the real world experiment. Collimated light is cast through pinhole on target on rotary stage. Camera captures images from opposite side. Our target is a plastic bin filled with gelatin. A blue plastic is stuck.

bounded by the physical constraint of the reconstruction.

We now look for an appropriate setup such that the coverage of the observation is high, while the center of the sinogram remains filled. From the discussion in Sec. 4.2.7, the coverage takes its maximum at $\theta_l = \frac{\pi - \theta_{FOV}}{2}$ in the case of perspective projection, however, in the case of $\theta_l > \frac{\pi - \theta_{FOV}}{2}$, the center of the sinogram is missing. For these reasons, the appropriate setup is $\theta_l = \frac{\pi - \theta_{FOV}}{2}$; however, care needs to be taken that θ_l does not exceed the angle.

4.4.2 Experiment on a real object

In this section, we perform an experiment in a real environment to confirm the validity of the shortest-path measurement by comparing the result with a measurement made under a parallel lighting setting.

The setup is shown in Fig. 19 for the shortest-path measurement; the target on the rotary stage is illuminated by the light source and captured by the camera from various angles. The target of the experiment is a bin filled with gelatin and blue transparent plastic struck at some distance from the center of the bin. The light is collimated with a lens and is narrowed by an aperture. θ_l is fixed to 45° . We chose the angle such that the center of the sinogram is filled while the observed intensity is high enough for a quick measurement.

To calculate the total absorption, a reference object without a plastic stick is measured in addition to the target; the total absorption is then calculated by Eq. (3). Note that this calculation also cancels out the angular nonuniformity of diffusion, or BTDF of the surface. Because s_t and s_r have ω_i and ω_o in common, the bidirectional transmission distribution function f_T of the surface of the target is cancelled out.

The next step is alignment of the light path. After a contour of the target is estimated considering the visual hull of silhouettes from various views, the light path is aligned with the contour estimated and a sinogram is generated. The interior is reconstructed from the sinogram.

For the comparison, we measure the same target under a parallel light setting. The same setup is used except that a parallel light source is cast directly and θ_l is set to 0° . The sinogram is generated directly from captured images under the assumption that rays travel straight in the target and measured transmitted rays remain parallel to each other.

Figure 20 shows sinograms of the parallel light setting and the shortest-path measurement. We cannot see an effect of plastic in the sinogram of the parallel light setting. This is because the parallel rays once diffuse at the surface when entering the target and light paths are mixed as illustrated in Fig. 12; therefore, rays passing through the plastic are no longer distinguished. In contrast, we see a clear trajectory through the plastic in the sinogram of the shortest-path measurement. There is also blurring along the trajectory and non-zero values

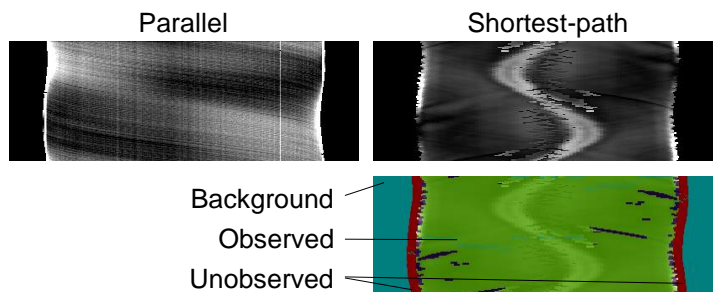


Figure 20. Acquired sinogram under parallel lighting and proposed measurement. We clearly see the trajectory of the plastic stuck in shortest-path measurement, which is hardly seen in parallel lighting.

outside the trajectory. This should be a result of corruption of the path due to scattering in the media and reflection and refraction at the plastic’s surface. We can also see small missing areas on both sides in the sinogram owing to the limitation of the measurement.

The result of reconstruction is shown in Fig. 21. From the top view of the target, the distribution of the absorption is expected as shown at top right. The red and blue lines in the figure respectively indicate the contour and the boundary between observed and unobserved areas of the sinogram.

We now look at the reconstruction of the parallel light setting that is reconstructed by the FBP. The distribution is almost uniform and we can hardly tell the area of the plastic stick. For the shortest-path measurement, we show two results of reconstruction obtained without optimization (i.e., the FBP) and with our optimization method. In contrast to the case for the parallel light setting, the proposed method successfully reconstructs the area of plastic stick regardless of the reconstruction method. This suggests that our path model approximates the actual paths well therefore the paths are converted to parallel by the alignment process. This confirms the validity of our assumption on light paths. There are blurry artifacts outside the plastic area that should be associated with the corrupted paths described above.

We now compare the results of the reconstruction methods. In the result of the FBP, the distribution outside the blue circle is not reconstructed and it corresponds to the missing area in the sinogram. In contrast, our optimization method

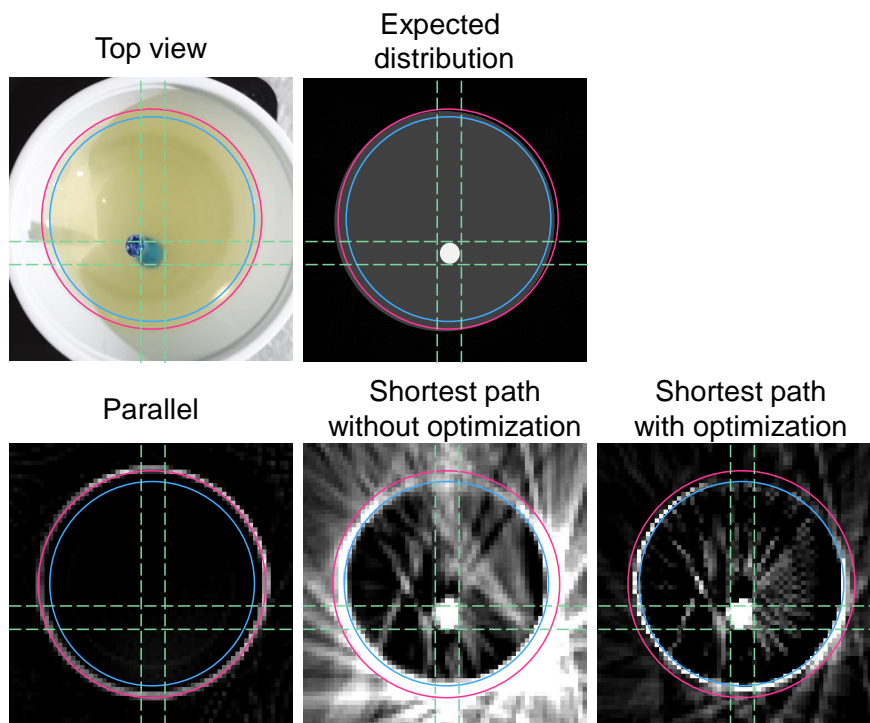


Figure 21. Expected distribution and reconstructed interior. While the interior is not reconstructed by measurement under parallel lighting, it is reconstructed with many artifacts by proposed measurement and reconstruction method without optimization. Reconstruction method with optimization successfully reduce artifacts significantly.

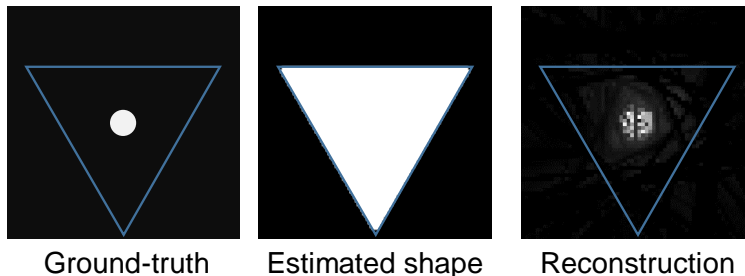


Figure 22. Measurement of the object with triangle shape. Our method is applicable to any convex shape.

is able to reconstruct the distribution where there are insufficient observations. It is confirmed that our method has an advantage over the FBP method.

4.4.3 Measurement of arbitrary convex shape

We perform a simulation experiment to show our framework works with an arbitrary convex shape. In this experiment, we simulate a measurement of a triangle pole. θ_l is set to 30° . Figure 22 shows the ground-truth, the estimated contour, and the reconstructed interior with optimization. A blue line shows the ground-truth contour of the object. In the estimated contour, the contour of the triangle is estimated almost correctly. Also, from the reconstructed interior, we can see the circular area at the center is reconstructed without a significant artifact.

4.4.4 Effect of scattering

Our method is based on the assumption of the shortest-path model that only the absorption of light in the object need be considered. However, as we found in the experiment for the real object, scattering in the medium may not be negligible in a practical measurement. It is expected that if the scattering of the medium is strong, our model is no longer a good approximation of paths of rays. In this section, we confirm the effect of scattering in a simulation environment.

In this experiment, the CT measurement is simulated with physically correct light transport. Synthetic data are generated by rendering with photon mapping algorithm[65]. The scene is shown in Fig. 23; i.e., a cylinder is illuminated by

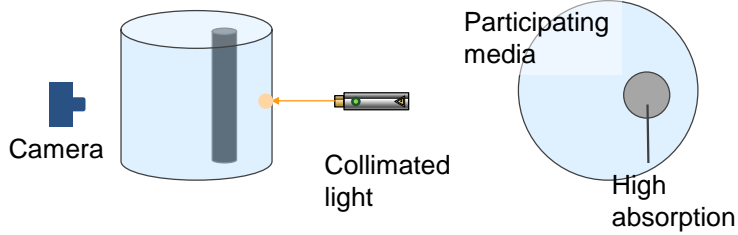


Figure 23. Illustration of the rendered scene. In this scene, we imitate the real-world experiment.

collimated light as in the experiment on the real object in Sec. 4.4.2. The cylinder is filled with the participating medium and there is another cylinder inside. The scattering of the media is isotropic and is parameterized with scattering coefficient σ_s and absorption coefficient σ . σ is set to zero in the outer cylinder and 10.0 in the inner cylinder. The refractive index of the media is set to 1.0.

CT measurements are performed for various scattering coefficients σ_s . Note that the radius of the cylinder is 1 and σ_s decides the mean free path of the ray according to $1/\sigma_s$. Figure 24 shows the top view and the projections on the camera for scattering coefficients σ_s of (i)1.0, (ii)2.0, (iii)3.0, and (iv)5.0. It is found that the projection is clear in (i), where most rays scatter once or twice, and the scattering degrades the projection as σ_s increases to 5.0, where rays scatter more than five times on average. The degradation of the projection directly reflects the quality of the raw and aligned sinograms as shown in Fig. 25. The bottom row shows the reconstruction from the aligned sinogram. We see that the degradation of the sinogram affects the reconstruction. While the highly absorbing part has a clear shape in (i), the shape is more blurry in (ii), (iii), and (iv).

The results show that our measurement is degraded by scattering; however, this can possibly be overcome using descattering techniques [66, 67].

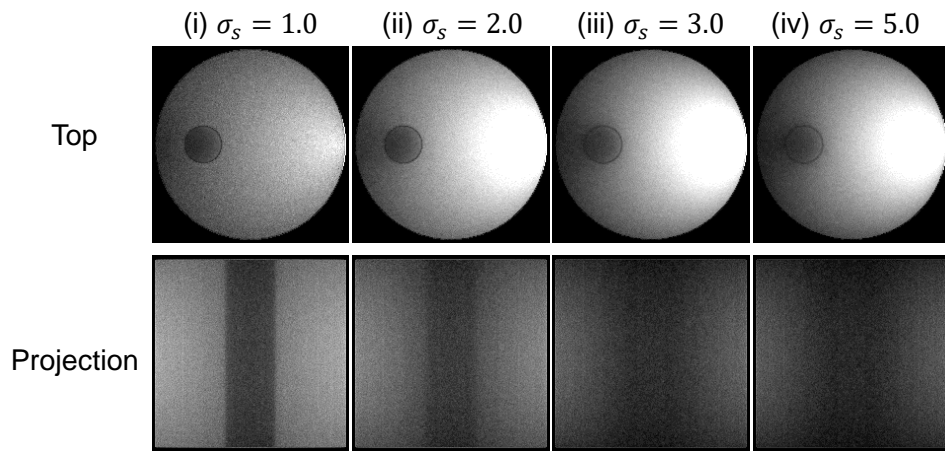


Figure 24. Top views and projections for different types of scattering. Because of the scattering, the projection of the inner obstacle is blurred.

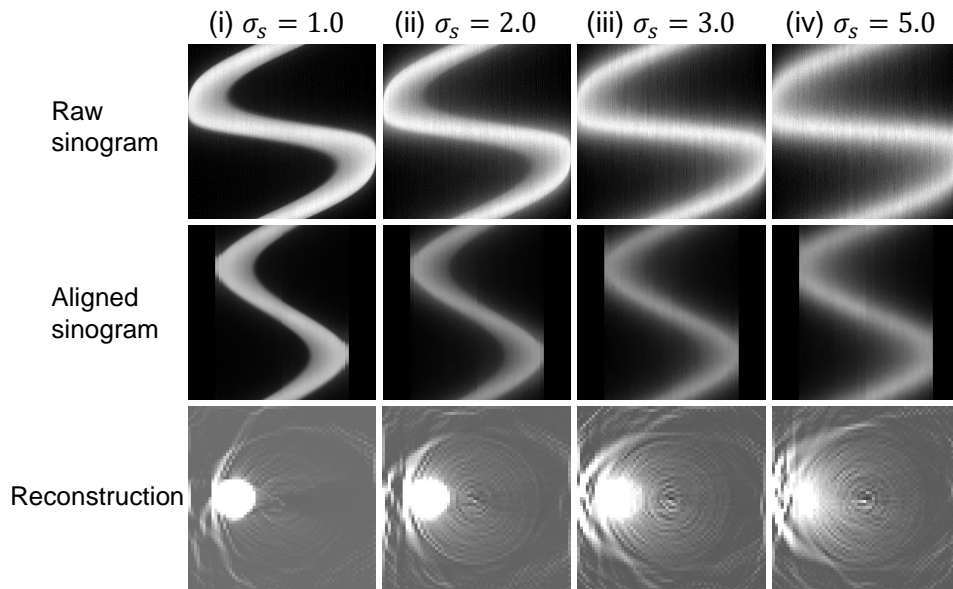


Figure 25. Sinogram and reconstruction for different scattering coefficients. The stronger scattering blurs measurement, resulting in degrading reconstruction.

4.5 Conclusion

We investigated the optical measurement of the internal structure of a diffuse-surface object. Our framework is built on the shortest-path model that assumes a ray only diffuses on the surface and travels straight inside an object. Our measurement is realized with a simple setup with a rotary stage, light source, and off-the-shelf perspective camera. It was found that the observation of light rays is never sufficient with this setup for the conventional reconstruction method. We solved this problem by introducing a reconstruction method based on numerical optimization. Because of the physical constraint on the light absorption and TV semi-norm regularization, the full interior could be reconstructed. Our method was shown to be able to reconstruct the interior of an object in a real world experiment. Furthermore, we evaluated the reconstruction with respect to the measurement setup. It was found that the reconstruction is not perfect if rays vital to the reconstruction are not observed. We also confirmed that scattering degrades the measurement; however, the measurement is still useful for a weakly scattering medium.

Currently, it is not easy to measure objects around us such like grapes that we took as an example in the Sec. 4.1. One of the difficulties is that a measurement of the surface BTDF requires additional measurement that is not always possible. Another problem is that amount of transmitted light is not enough for highly absorbing target. Both a measurement and a prototype need further improvement for more practical measurement.

5. Light transport acquisition of projector camera system

5.1 Introduction

In this chapter, we acquire the light transport in the projector-camera system. The projector camera system is one of the common system for the active measurement in the computer vision, used for tasks such as 3D triangulation, super-resolution, and projection-mapping.

As we discussed in Sec. 2, light transport in projector camera system is received light of camera pixels when each projector pixel is turned on. Since today's projector and camera have high resolution, the number of sampling is enormous.

5.1.1 Distance of light transport

The light transport is characterized by the transport distance or the distance the light travels in the scene as illustrated in Fig. 26. Direct transport, that is shown in red line, is the transport of the light that bounce only once in the surface of the object as with diffuse reflections. In short range transport, that are shown in orange lines, the light that travels short distance as a result of subsurface scattering or diffuse inter-reflections. The light that travels long distance as with specular inter-reflections is considered as long range transport, that is shown in yellow line in the figure.

In this chapter, we aim to acquire the light transport according to its distance to analyze the light behavior in the scene. While the transport distance is meaningful information, it is difficult to acquire the light transport of the specific distance efficiently under spatially varying illumination. Let us explain this problem using Fig. 27. For the point C_A in the scene, the illumination I_A corresponds to the specific transport distance d . And for the different point C_B , the illumination I_B corresponds to the same distance. Therefore, two measurements are required to acquire the transport of the same distance for two points.

Reddy et al.[68] show the light transport can be decomposed into direct, near-range, and far-range transport (which corresponds to direct, short, and long transport respectively in our notation) components. They decompose the light

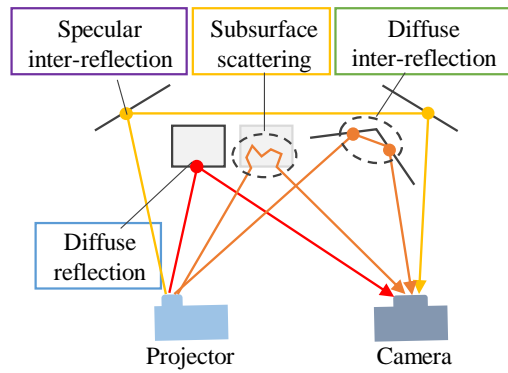


Figure 26. The light transport is characterized by the transport distance. The transport distance depends on optical behaviours, such like diffuse reflections, diffuse inter-reflections, subsurface scattering, and specular inter-reflections.

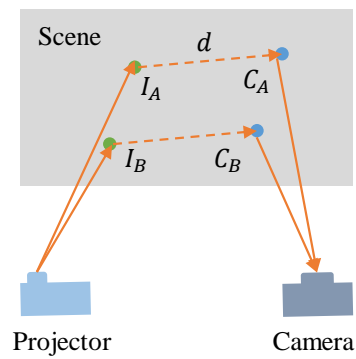


Figure 27. Corresponding illumination for the same transport distance at different points. To acquire the light transport of the same distance at two different points, two measurements are required.

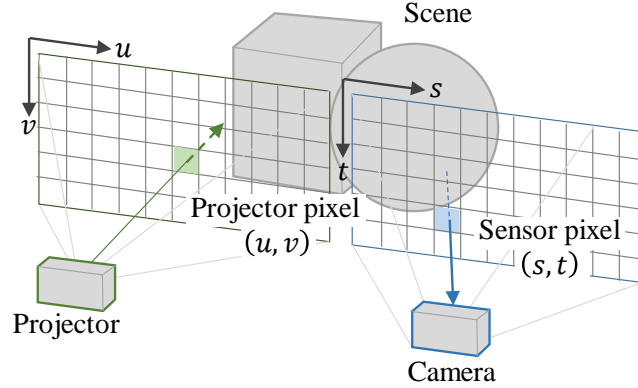


Figure 28. Full light Transport between projector and camera is described in 4D function.

transport into three components by high- and low- frequency patterns, however, their method does not acquire the light transport of the specific distance.

5.1.2 Light transport in projector camera system

In projector camera system shown in Fig. 28, light cast from the projector interacts with the scene, then received by the camera sensor. Projector send a ray to a specific pixel which is expressed as (u, v) in a projector plane and camera receive a ray through a specific pixel which is expressed as (s, t) in a sensor plane. Therefore, the light transport between projector and camera is fully expressed by 4D function $T_{full}(u, v, s, t)$.

In this chapter, the light transport distance is defined in a camera plane where 3D scene is projected. Therefore, short light transport in our measurement does not always mean short distance in 3D coordinate. For instance, pixels which are located in close distance could point to far 3D locations at different depths. Note that short distance is 3D coordinates always satisfies short distance in our measurement unless Cartesian distance is used.

5.1.3 Our contribution

In this chapter, we propose the efficient acquisition that the light transport of the specific distance is acquired for all the sensor pixels by small number of

measurements. Such acquisition is made by utilizing using *synchronized projector camera system* without any computation. We propose new imaging technique which exploits the light transport between the illumination plane and camera pixels, called *plane-to-ray* light transport. Then, we extend it to acquisition of full light transport.

We explain the acquisition of plane-to-ray light transport in Sec. 5.2 and acquisition of full transport in Sec. 5.3. We show acquired light transport and applications for both light transport in Sec. 5.4, and concludes in Sec. 5.5.

5.2 Acquisition of plane-to-ray light transport

5.2.1 Epipolar geometry and light transport

We utilize the setup of synchronized projector camera system [69], that consists of a raster-scan projector and a rolling-shutter camera. The projector illuminates the scene with a plane that is swept vertically. The camera synchronizes its rolling shutter to a fixed row-offset from the illumination plane. Each camera row exposes as projector row advances, so that a single image is formed.

The Projector and camera are rectified so that their rows are aligned on the same epipolar plane. In [69], the direct and indirect transport is acquired using this alignment. Since direct light, that bounce only once in the scene, must travel through the same epipolar plane, it can only travel from projector row i to camera row i . In contrast, indirect light, that multiple times, can travel from projector row i to any camera row j except i .

This alignment also allows us to acquire the light goes through the epipolar plane which contains the projector row v and that returns through the another epipolar plane contains the camera row s . We propose a new light transport, called *plane-to-ray light transport*, characterized by the relative row offset between projector row v and camera row s .

We illustrate plane-to-ray light transport in Fig. 29. Plane-to-ray light transport is transport between the projector row v and a sensor pixel (s, t) in camera row t , that is expressed as 3D function $T_{PTR}(v, s, t)$. The row offset between projector row v and camera row s is controlled by the *synchronization delay*, the timing difference between the synchronized projector scanning and camera rolling shutter. In addition, the *exposure* of the camera row determines the width of illuminated area.

We show the effect of delay and exposure in Fig. 30. A regular image of the scene is shown in (Fig. 30(a)). When $t_d = 0$, the image is identical to epipolar image in [69] so that only direct light is captured. When $t_d = 1200us, t_e = 450us$, the indirect light (inter-reflections caused by mirror-ball) is captured(Fig. 30(c)). The band increases as exposure is increased to $t_e = 2000us$ (Fig. 30(d)).

In an ideal planar illumination system, one could capture the light transport by projecting one line at a time and taking an image. However, this impulse

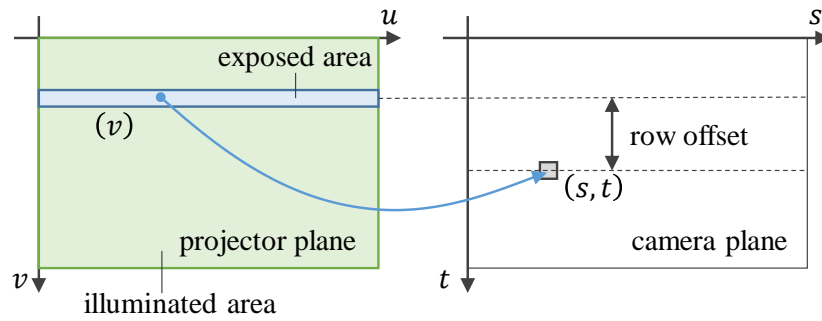


Figure 29. We define plane-to-ray Light Transport as transport between an illuminated row and a camera pixel.



(a) regular



(b) $t_d = 0us, t_e = 300us$



(c) $t_d = 1200us, t_e = 450us$



(d) $t_d = 1200us, t_e = 2000us$

Figure 30. Indirect image captured with various delay and exposure. (b) At $t_d = 0us$ direct reflections are captured (epipolar imaging). (c) At $t_d = 1200us$, light transport of specific distance is captured, (d) and its bandwidth is widened by choosing longer exposure t_e .

scanning suffers from low SNR due to low light levels [70]. This would particularly affect the capture of light paths such as subsurface scattering and long-range indirect light. In addition, in a real system, the laser itself has a temporal jitter, which may cause light to leak into neighboring rows as noticed in [69]. To solve these issues, we use light multiplexing as a way to increase the SNR for light transport acquisition.

In our imaging system, we utilize a rolling shutter camera to capture these planes of light. Our key insight is that this rolling shutter, synchronized to the projector, performs light multiplexing for planar illumination. We now proceed to describe this light multiplexing using the parameters of delay and exposure in a rolling shutter system.

5.2.2 Light Multiplexing using Delay and Exposure

For a rolling shutter camera synchronized to the epipolar illumination of the projector, we can control the delay and exposure of this shutter to perform light multiplexing. The exposure determines the number of rows being exposed with larger exposures leading to larger sets of rows being exposed. The delay is the distance between the illuminated projector row and the center of the exposed rows.

The rolling shutter of the camera can be synchronized to the projector illumination, as described in [69]. In particular, this means the pixel clock is fixed and focal length of the lens adjusted so that the projector rows and camera rows change with the same vertical velocity. In epipolar imaging mode, the delay is zero, so that the band of exposed camera rows is on the same epipolar plane as the light being projected, while in non-epipolar mode, the band of exposed camera rows does not include the epipolar plane where the light is. Light multiplexing occurs since each row gets light from multiple projector lines due to the width of the exposure and the value of the delay. To describe the demultiplexing algorithm necessary to estimate 3D light transport, we first must derive the relationship between delay and exposure, and use it to model the illumination.

Relationship between delay and exposure: We use the same notation as [69] to parametrize delay and exposure in a rolling shutter system. Let t_p denote

the amount of time for which the projector illuminates a single scanline (with some finite band width), t_e be the exposure time which corresponds to a contiguous block of rows being exposed, and t_o denote the time offset of synchronization between the projector and camera. Additionally, we denote t'_o as the time difference between the start of exposure and when the projector illuminates that row of pixels. Please see Figure 31 for a visual description of these parameters.

As we change t_o , this changes t'_o , and thus we express delay: t_d as the difference between the center times of exposure and illumination, as following:

$$t_d = \frac{1}{2}t_e - \frac{1}{2}t'_o. \quad (31)$$

Positive $t_d > t_e/2$ means the camera row receives light from a vertically lower epipolar plane. Similarly, negative $t_d < -t_e/2$ means the light arrives from a vertically higher epipolar plane. If $0 \leq |t_d| \leq t_e/2$, then the exposed row receives a majority of illuminated light from the same epipolar plane. Typically, epipolar imaging operates with $t_d = 0$ and t_e as short as possible (as shown in Fig. 31(c)).

Illumination Model: We formulate a model for the illumination as a function of delay and exposure. Using calibration, we obtain the speed of the projector scanline v_p sec/line in the scene. Given this, we express illumination band width I_w and its center location I_d by the following equations:

$$I_w(t_e) = v_p t_e, \quad I_d(t_d) = v_p t_d. \quad (32)$$

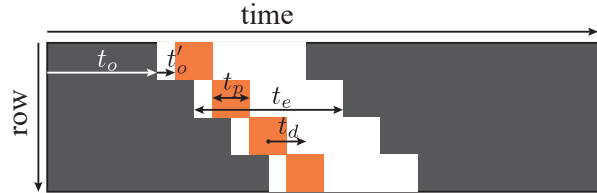
Let v denote a row of the projector plane. We then define the illumination function $L(v, t_d, t_e)$:

$$L(v, t_d, t_e) = \begin{cases} 1, & \text{if } \|v - I_d(t_d)\| < \frac{1}{2}I_w(t_e); \\ 0, & \text{otherwise.} \end{cases} \quad (33)$$

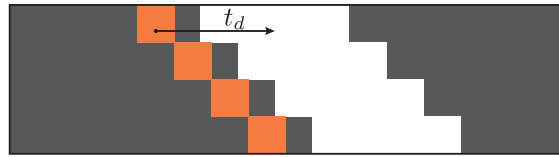
Note that we define the maximum intensity of the projector as 1.

Demultiplexing: Now, we perform illumination demultiplexing and estimate 3D light transport in the scene. For given t_d and t_e , the observation I at pixel (s, t) is given by a convolution of the illumination with the light transport operator:

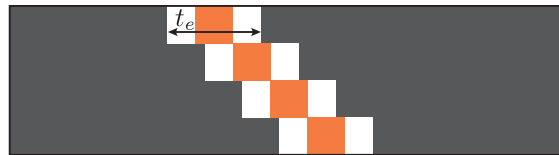
$$I(s, t) = L(v, t_d, t_e) * T(v, s, t). \quad (34)$$



(a) The projector illuminates a single row for a time t_p in orange. At the same time, the rolling shutter exposes a single row for length t_e . Light from a single row (orange) will be captured not just by the same camera row, but rows above and below it that are being exposed (white). Delay t_d is the distance from center of exposure to the center of illumination. t'_o is the time between start of exposure and illumination in a row, and t_o is the synchronization offset from projector to camera.



(b) As the delay is increased, the illuminated projector row sends light to camera rows that are at least one row above it. This corresponds to short range non-epipolar light paths in the scene.



(c) As the exposure is decreased, the illuminated projector row leaks less light into neighboring rows, resulting in a majority of epipolar light paths captured.

Figure 31. Timing diagram of projector illumination and camera rolling shutter for epipolar imaging.

Note that, $T(v, s, t)$ is 3D light transport from row v to a pixel (s, t) . This relationship is illustrated in Fig. 29. We note that this equation can be discretized to the standard matrix-vector product of light transport.

We can write the epipolar and non-epipolar images by the following convolutional equations:

$$I_e(s, t) = \delta(t - v) * T(v, s, t), \quad (35)$$

$$I_n(s, t) = (1 - \delta(t - v)) * T(v, s, t). \quad (36)$$

Hence, if we can estimate T from the image stack of varying t_d and t_e , we can synthesize epipolar and non-epipolar images. We denote the i -th image with delay $t_{d,i}$ and exposure $t_{e,i}$. Thus we estimate the light transport T^* as the solution to the following optimization problem:

$$\min_{T(v,s,t)} \sum_i^N \|I_i - \{L(v, t_{d,i}, t_{e,i}) * T(v, s, t)\}\|_2^2 + \alpha E_c + \beta E_s,$$

subject to $T \geq 0, \forall v, E_c = \|\frac{\partial}{\partial v} T\|_2^2, E_s = \|T\|_1.$

We use additional regularization for smoothness and sparsity in the light transport: α and β are coefficients of smoothness and sparsity respectively. This helps with the optimization to reduce noise and other image artifacts. The total number of images in the stack is N . In practice, we utilize $\alpha = 0.01$, $\beta = 0.01$, and $N = 75$.

Since the formulation is per-pixel, the optimization is easily parallelizable. We use the CVXPY framework for convex optimization to solve this [71]. We feed most delay-exposure images to the solver except for those delay images which lie on the boundary between epipolar and non-epipolar imaging ($t_d \approx t_e/2$), which have significant horizontal artifacts due to synchronization problems. One limitation of our algorithm is the sparsity condition prevents recovering dense light transport effects.

5.2.3 Delay-Exposure Image Stacks

We thus capture a series of images while varying delay t_d and exposure t_e . We typically use uniformly sampled points between minimum and maximum values for both delay and exposure as part of our sweep.

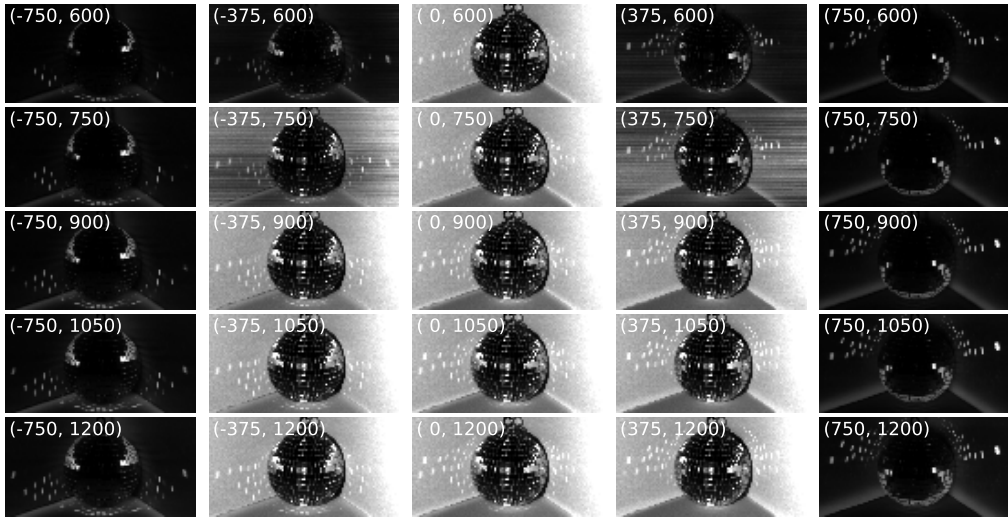


Figure 32. An image stack. Transport distance depends on delay, and bandwidth depends on exposure.

By controlling the delay and exposure, we have the ability to capture short and long-range non-epipolar light. As the delay increases, light from the illumination plane has to travel a longer vertical distance to reach the camera row. This gives a minimum bound of the optical path length traveled by the indirect light. By controlling the exposure, we can allow more or less amount of light that has traveled this minimum bound, thus creating a *band* of non-epipolar light. This corresponds to banded diagonals off the main diagonal in a light transport matrix [69, 72].

An example of image stack is shown in Fig. 32. We visualize the specular inter-reflections of a disco ball shifting vertically as the delay changes.

Noise is primarily determined by the amount of light reaching the pixels (although there are synchronization artifacts at very short exposure times due to jitter in the laser raster scan). For indirect imaging, specular inter-reflections (such as the disco-ball reflections) are brighter and thus less noisy than diffuse inter-reflection or subsurface scattering effects. Since exposure is coupled to the band of light received by the rolling shutter, there is a trade-off between integrating more light and the tightness of the band of indirect light (i.e. the resolution of the illumination function).

5.2.4 Efficiency of light transport acquisition for limited range

The light transport can be expressed as a light transport matrix whose row corresponds to the sensor index and column corresponds to the illumination index. We discuss about the efficiency for limited range transport, by taking an example of short-range light transport.

First, we explain the order of the acquisition using a sub-matrix of the light transport matrix. In Fig. 33, we visualize the sub-matrix of the light transport matrix, where each column of the matrix is the projector row and each row is the sensor row. The diagonal elements are the direct component where the light from a row of the projector reaches the same row of the sensor. The adjacent elements in the row direction are the short-range transport.

Now, we assume the scene has the direct and short range transport that is expressed as Fig. 33(a). To explain the effectiveness of the measurement, first, let us consider about how the transport is acquired by pixel-to-pixel measurement. In pixel-to-pixel measurement, a pixel of the projector is turned on, and all the sensor pixels are exposed with global-shutter. Each acquisition fills a column of the matrix (Fig. 33(b)). Therefore, it requires all the rows to be acquired to obtain the direct and the short-range transport. In contrast, our method acquires an oblique element in each capture (Fig. 33(c)). It requires only few captures to acquire the direct and the short-range transport.

There is a trade-off between the range of transport captured at once and the number of captures. In short, both methods require the same number of captures to acquire all the elements of the matrix. Our method is beneficial when the range of the transport is limited as for short-range transport.

Short-range transport is also assumed in [47]. They parallelized the acquisition by subdividing the projector pixels into blocks to make sure a sensor pixel is affected by only one illumination block. In our method, there is always only one illuminated row, thus no need to subdivide the projector rows.

5.3 Acquisition of full light transport

We extend acquisition of plane-to-ray light transport to the acquisition of the full light transport. In the acquisition of plane-to-ray light transport, a white pattern

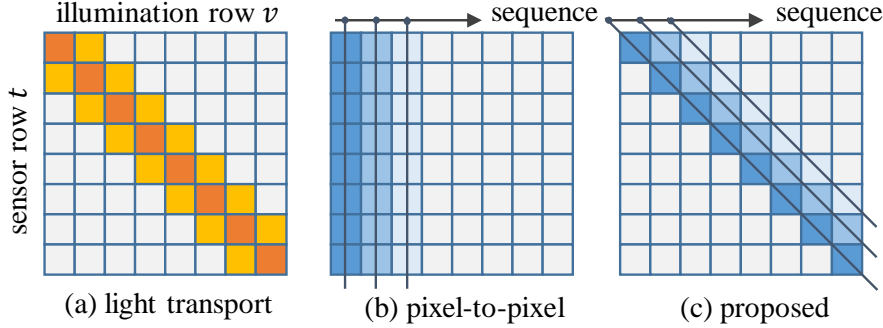


Figure 33. Light transport matrix and the order of the acquisition. For the acquisition of light transport in scene (a), pixel-to-pixel measurement (b) is not efficient because it acquires light transport from a specific illumination row to all sensor rows at a single frame.. In contrast, proposed measurement acquires light transport from illumination rows to sensor rows of the specific transport distance at a single frame.

is projected to illuminate all the pixels in the projector row. To acquire the light transport from a pixel from the projector instead of a projector row, we project a vertical line instead of the white pattern as shown in Fig. 34. Since a pixel is only illuminated during exposing a camera row as shown in Fig. 35, the light transport $T_{full}(u, v, s, t)$ from a projector pixel (u, v) to a camera pixel (s, t) is acquired.

5.3.1 Illumination multiplexing

For fine acquisition of the light transport, the width of the illumination should be small. The illumination with a too small width causes low SNR. To avoid this problem, we acquire the transport with larger width and demultiplex to reconstruct the transport with a smaller width.

We formulate the illumination function. The illumination function is defined on the projector plane as shown in Fig. 36. The illumination is modeled as a function of synchronization delay t_d and exposure t_e . Let v_p be the speed of the projector scanline. The center of the illumination along v -axis I_d and the

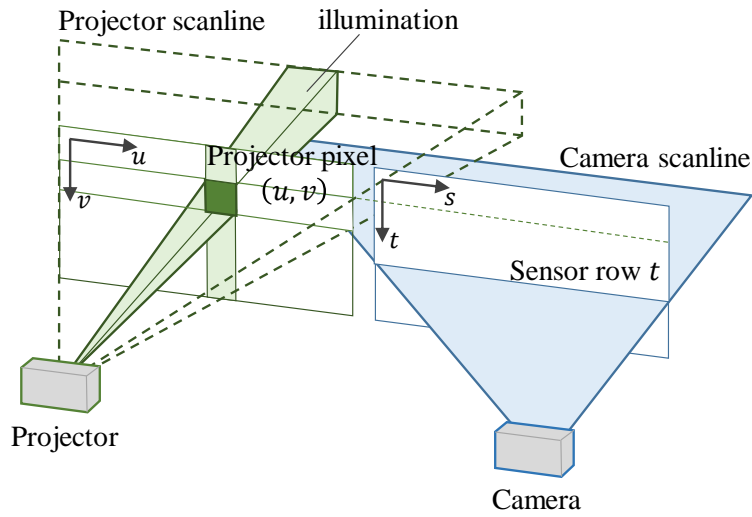


Figure 34. Illustration of full light transport acquisition. A vertical stripe is employed to limit the illumination area to the certain pixel.

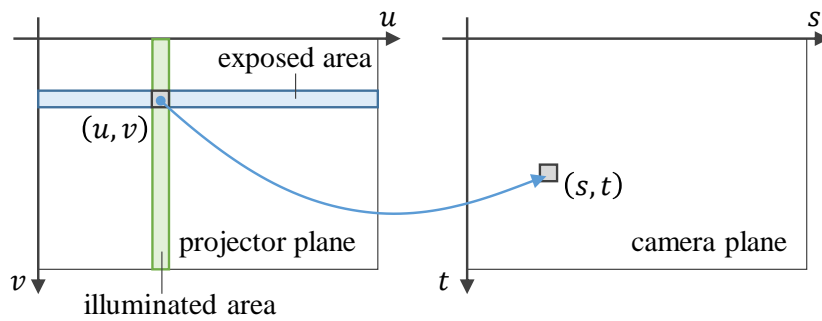


Figure 35. Full Light Transport is defined as transport an illuminated pixel to a sensor pixel.

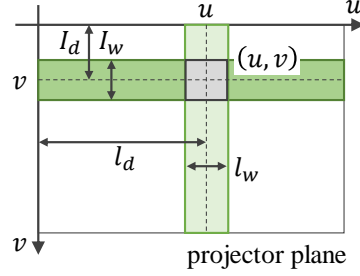


Figure 36. Illustration of illumination function.

illumination width along v -axis I_w are given by

$$I_d = v_p t_d, \quad I_w = v_p t_e. \quad (37)$$

Similarly, we introduce center location of line along u -axis l_p and line width along u -axis l_w to control a vertical line. We define the illumination function $L(u, v; l_p, l_w, t_d, t_e)$ as

$$L(u, v; l_p, l_w, t_d, t_e) = \begin{cases} 1, & \text{if } \|u - l_p\| < \frac{1}{2}l_w \text{ and } \|v - I_d\| < \frac{1}{2}I_w \\ 0, & \text{otherwise.} \end{cases} \quad (38)$$

Let $I(s, t)$ denote the observation at a sensor pixel (s, t) . The observation is a convolution the light transport $T(u, v, s, t)$ with the illumination function $L(u, v; t_d, t_e, l_d, l_w)$, then is expressed by

$$I(s, t) = \{L(u, v; t_d, t_e, l_d, l_w) * T(u, v, s, t)\}_{u,v}. \quad (39)$$

Since the illumination function is known, the light transport \hat{T} is reconstructed by

$$\arg \min_{T(u,v,s,t)} \left\| I(s, t) - \{L(u, v; t_d, t_e, l_d, l_w) * T(u, v, s, t)\}_{u,v} \right\|. \quad (40)$$

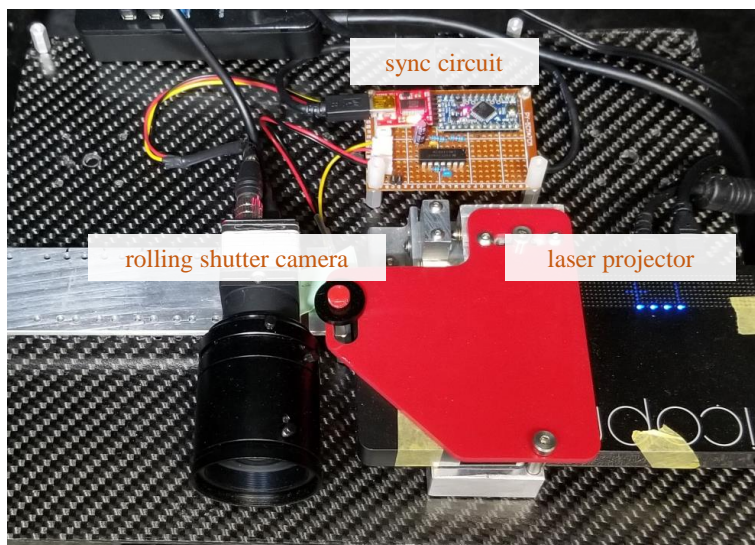


Figure 37. Prototype. Rolling shutter of the camera and the raster-scan of the projector is synchronized by sync circuit.

5.3.2 Hardware

We use a prototype as shown in Fig. 37. A Celluon PicoPro projector (resolution 1280×720) and an IDS UI-3250CP (resolution 1600×1200) are aligned on the same plane in parallel with a baseline of 50 mm. The rolling shutter is triggered by the VSYNC signal generated by the projector after being processed by the sync circuit. The speed of the projector scanline $v_p = 5.89 \times 10^3$ is obtained by counting a number of illuminated rows during fixed exposure.

5.4 Experiments

5.4.1 Analysis of light behavior

Analysis using plane-to-ray light transport For each pixel, we can plot the pixel intensity as a function of the delay t_d . We call this a *delay profile*, and it yields information about the scattering of light with respect to the planar illumination of the projector. Delay profiles look qualitatively different for sub-surface scattering and diffuse interreflections, which are short-range indirect light effects, versus specular interreflection that has long range. We note that Wu et al.

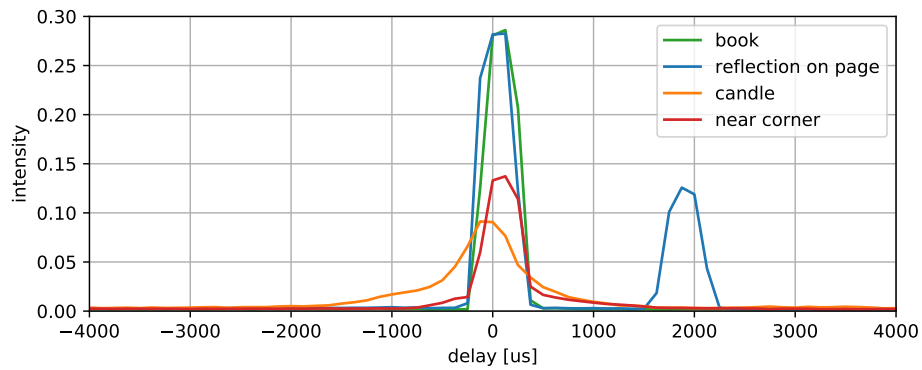
performed a similar analysis using temporal delay for time-of-flight imaging [73].

In Figure 38, we image a scene with a variety of these effects and show their delay profiles. Note how subsurface scattering material like the candle has a wide broadening profile (orange), while diffuse interreflection in the near corner has a steeper profile (red). The diffuse reflection from the book page itself has an unimodal peak (green), but the specular interreflection has a bimodal peak (blue). Note how specular interreflections from the mirror ball (blue) have two peaks in their delay profile. This is due to a diffuse reflection from the page at $t_d = 0$ coupled with a peak from the specular reflection of the mirror ball. For the near corner of the book (red) and candle (yellow), their broadened delay profiles are due to subsurface scattering. The more translucent the object, the more broader its delay profile (see also milk results in Section 5.4.9). Note that the delay profiles are not symmetric around zero as one would expect, but are affected by the surface geometry/surface normal at those points. This relationship between symmetry and surface normal is a subject of further investigation.

Analysis using full light transport Using full light transport, we can perform more detailed analysis. In the case of full light transport, the profile at each pixel is two dimensional since it is a slice of $T_{full}(u, v, s_0, t_0)$, where s_0, t_0 are fixed to camera pixel. In Fig. 39, we show the profile of the different light transport in the scene. The diffuse reflection from the book has clear rectangle shape (blue), since it is almost an impulse response to the rectangle illumination; Note that the delay profile has a clear unimodal peak. The subsurface scattering from wax candle (yellow) has larger extent compared with the surface of the book, and is isotropic. In the profile of diffuse inter-reflection from the corner of the book (green), we can see the advantage of the full light transport. It has large extent in the horizontal direction since the inter-reflection takes place between the left and right pages, therefore we can know the direction of inter-reflection. Also, the value of profile gradually decreases according to the distance from the center because the effect of the diffuse inter-reflections is depend on the distance between the surface. Finally, the specular inter-reflection from the disco-ball (purple) shows two independent clear peaks in the profile. From the profile, we can know the spatial relationship of the source of inter-reflection.



(a) scene



(b) delay sweep profile

Figure 38. Delay sweep profiles of various kinds of light behavior. While the book (green) has only one peak, the reflection on book (blue) has two peaks due to inter-reflection. Candle (orange) has wider profile due to subsurface scattering, and there is effect of diffuse inter-reflection between pages near corner (red).

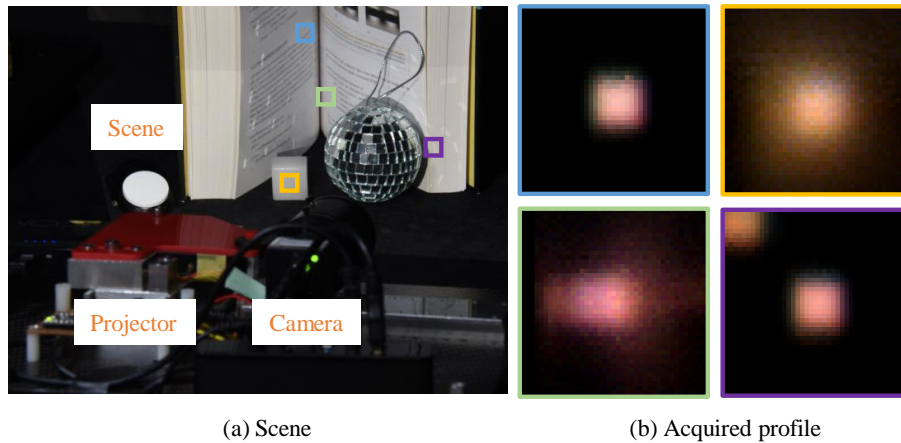


Figure 39. Two dimensional profiles for various kinds of light behavior. They provides a spatial response that is useful for detailed analysis.

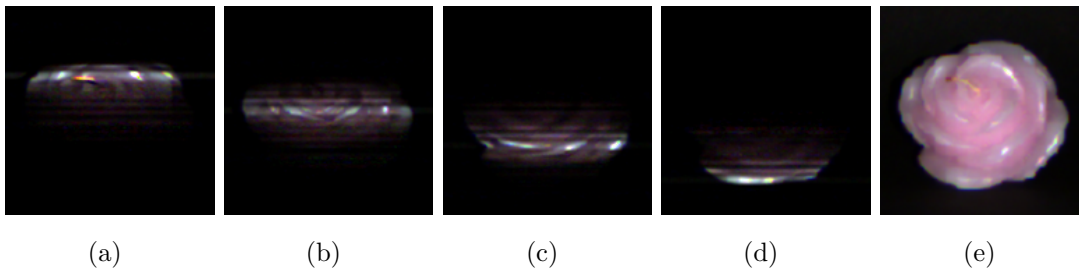


Figure 40. We show relit images under virtual single line illumination sweeping from up (a) to bottom (d). The regular image is shown in (e).

5.4.2 Relighting

Relighting using plane-to-ray light transport Plane-to-ray light transport allows us to synthesize novel images. For instance, we can render a new image with a novel illumination pattern of any linear combination of projector rows using the T operator. In Figure 40, we synthesize relighting from a single line illumination for the imaged rose.

Relighting using full light transport The full light transport also allow us to relight the scene with arbitrary illumination pattern that is not limited to horizontal line in the case of plane-to-ray light transport. In this experiment, we light the scene using the full light transport to evaluate the acquisition, by

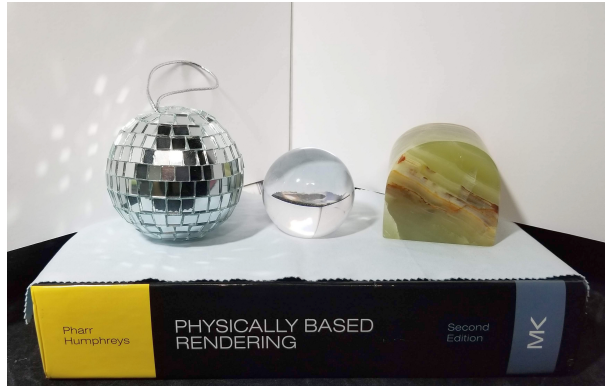
comparing with pixel-to-pixel measurement.

In Fig. 41, we synthesize the relit image with a checkerboard pattern illumination. In pixel-to-pixel measurement, rectangle patterns are projected sequentially and captured by the global shutter camera. We use exposure $t_e = 170\mu s$ for both cases. For our method, we use $l_d = 0\text{px}$ to $l_d = 900\text{px}$ at every 20px , $l_w = 40\text{px}$, $-1,700\mu s$ to $1,700\mu s$ at every $170\mu s$. Correspondingly, for the naïve method, a rectangle pattern ($20 \times 20\text{px}$) is projected repeatedly with the shift of 20px along u and v axes. We show the relit results of pixel-to-pixel and proposed measurement in Fig. 41(b) and Fig. 41(c), respectively. Both methods produce almost the same relit images, even at refracted light in glass ball or at subsurface scattering on the marble. Note that pixel-to-pixel measurement requires 3,726 measurements while our method requires only 506 measurements.

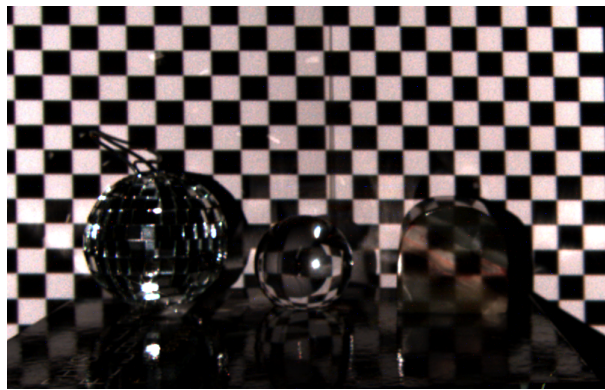
5.4.3 Improving SNR by Multiplexing

Case of plane-to-ray light transport In this experiment, we validate the effect of illumination multiplexing. For this single line relighting of the same scene of Sec. 5.4.2, we compare our method in Fig. 42(a) versus conventional imaging techniques. We show the comparison against a single projected line with exposure of 16ms in Fig. 42(b), and a single line projection with exposure of 800ms in Fig. 42(c). Note that our method achieves better noise performance than Fig. 42(b) since we utilize multiplexed illumination to capture our delay-exposure stack. Our method achieves similar performance to Fig. 42(c) in terms of noise, but requires multiple images and does not capture the long range light transport effects for far away rows due to the sparsity assumption in our optimization.

Case of full light transport We evaluate the effect of the illumination multiplexing for the case of the full light transport. In this experiment, we acquire the light transport under high-frequency illumination (square illuminations with the size of 10px in projector plane). For measurement without multiplexing (*simpler* measurement), we use $l_w = 10\text{px}$, $l_d = 5\text{px}$ to $l_d = 1,275\text{px}$ at every 10px , $t_e = 170\mu s$, and $t_d = -850\mu s$ to $t_d = 850\mu s$ at every $170\mu s$. In relighting results with checkerboard pattern (Fig. 43(a)) and with floodlit in which all the noises contribute (Fig. 43(b)), colored granular noises appear everywhere since



(a) Scene

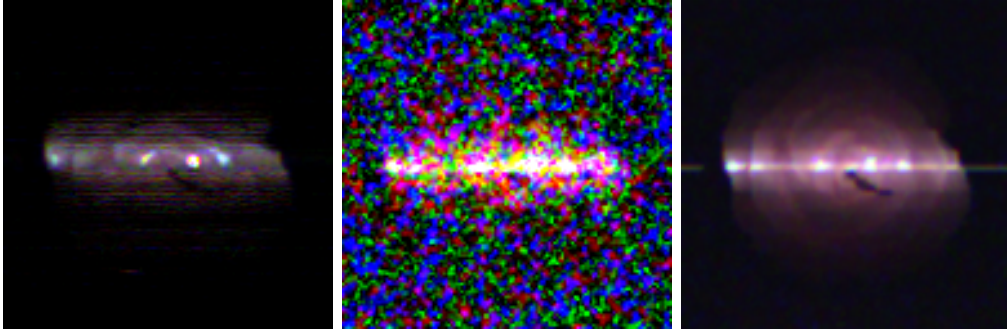


(b) pixel-to-pixel



(c) Proposed

Figure 41. Relighting under virtual checkerboard pattern illuminations from full light transport. Proposed method successfully relights the scene with less number of measurement, even the refraction in glass or subsurface scattering on the marble.



(a) Synthesized Result (b) Actual single light projection at 16ms (c) Actual single line projection at 800ms

Figure 42. Effect of illumination multiplexing for relighting with virtual single line. Synthesized result contains less noise while actual single light projection at short exposure is noisy.

the sensor noise is amplified.

For multiplexed measurement, we use $l_w = 50\text{px}$ and $t_e = 850\mu\text{s}$, which are five times larger than the simplex measurement, and l_d and t_d are set to the same value as the simplex measurement. In the relighting results with checkerboard pattern (Fig. 43(c)) and with floodlit (Fig. 43(d)), the noises are clearly reduced. The amount of light is 25 times larger in each capture while the number of captures is the same for both measurements. Since the sensor noise is constant for each capture, the multiplexing improves SNR.

5.4.4 Efficient Acquisition of Short Range Transport

In this experiment, we evaluate a transport range covered in our measurement by changing the delay range. We acquire the full light transport for this evaluation. We capture the scene with a disco-ball, a glass ball, and marble, where each of them contributes to inter-reflection, refraction and subsurface scattering respectively. We use $|T_d| < T_{d\text{max}}$ at every $170\mu\text{s}$. We render the floodlit images for the cases of $T_{d\text{max}} = 0, 850, 1700,$ and $2550\mu\text{s}$ as shown in Fig. 45. The inter-reflections appear on the wall are increasing, according to $T_{d\text{max}}$. Also, we can see that the illumination on the wall that is seen through the glass ball is changing. The appearance of the marble looks almost same except for $T_{d\text{max}} = 0$.



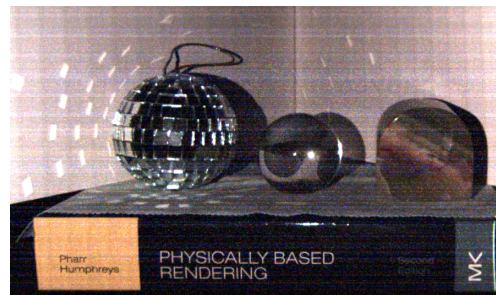
(a) Simplex (high frequency)



(b) Simplex (floodlit)



(c) Multiplex (high frequency)



(d) Multiplex (floodlit)

Figure 43. Effect of illumination multiplexing for relighting with virtual patterns. While simplex measurement is suffered by noisy measurement, multiplex measurement successfully reduce the noise.

We visualize the light transport in the scene (Fig. 44) between the columns 1, 2, and 3 of the projector to the corresponding column of the camera in Fig. 46. In the matrix of the column 1, the diagonal elements have high value because most of the light is reflected directly on the wall. In the row corresponding to r_1 , however, the highest value is not in the diagonal elements since the inter-reflection due to the disco ball appears at this pixel. The high value appears in the row close to the diagonal line since this inter-reflection is a relatively short range transport. In the matrix of the column 2, we can see the effect of refraction. r_2 and r_3 are the pixel of the top and the bottom of the glass ball. In the rows between r_2 and r_3 , it takes high value along a line from left-bottom to right-top since the incident light that enters the ball at the upper part reaches the lower part at the opposite side due to the refraction. In the matrix of the column 3, we can see the effect of subsurface scattering. r_4 and r_5 are the pixel of the top and the bottom of the marble. While the diagonal elements take high value in the matrix, adjacent several rows also have a relatively high value. This is because some light travels inside the object and reaches a different point of the surface due to subsurface scattering.

The parameter of the measurement T_{dmax} decides how many adjacent rows of the diagonal elements are acquired. Setting T_{dmax} to small value means the elements only close rows to the diagonal elements are acquired and the far range transport is not acquired.

5.4.5 Sharpening epipolar imaging

Demultiplexing to plane-to-ray light transport allows us to shapen epipolar imaging. In epipolar imaging, there is an inherent trade off between the amount of non-epipolar light that leaks into the signal and exposure t_e . Thus it is difficult to capture epipolar images with large exposure as the amount of non-epipolar light inside the epipolar image scales with $t_e - t_p$.

However, as noted in Equation 36, if we can resolve light transport to a fine resolution in projector rows v , we can synthesize a “sharper” epipolar image. We can computationally render an epipolar image to the limit of the light’s illumination width I_w .

In Figure 47, we image a rose candle made of translucent wax. We synthesize

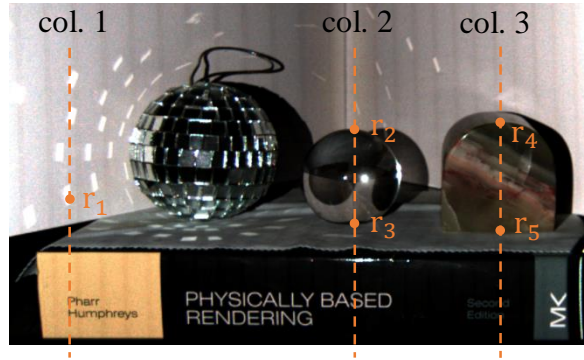


Figure 44. Scene with wide range of light transport, including inter-reflections, refraction, and subsurface scattering.

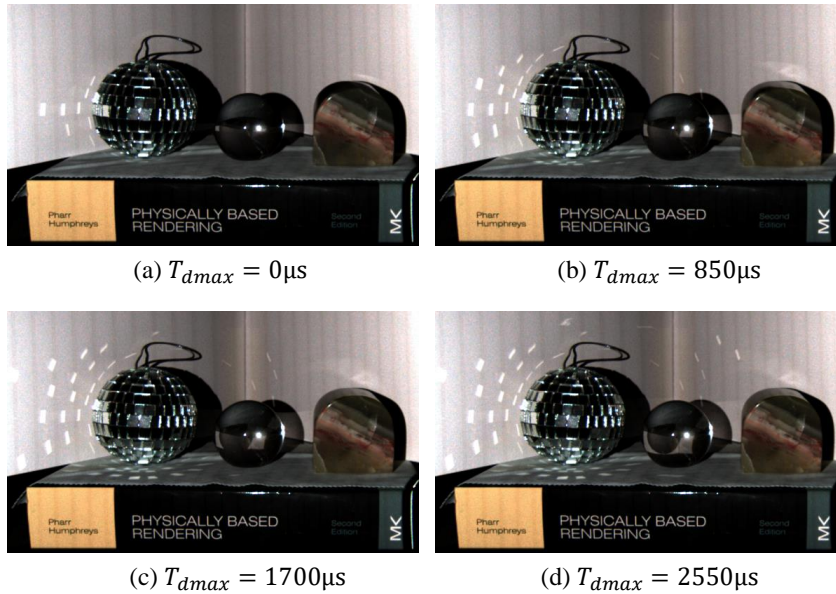


Figure 45. Appearance according to Delay Range. Range of transport distance of captured light transport increases according to delay range.

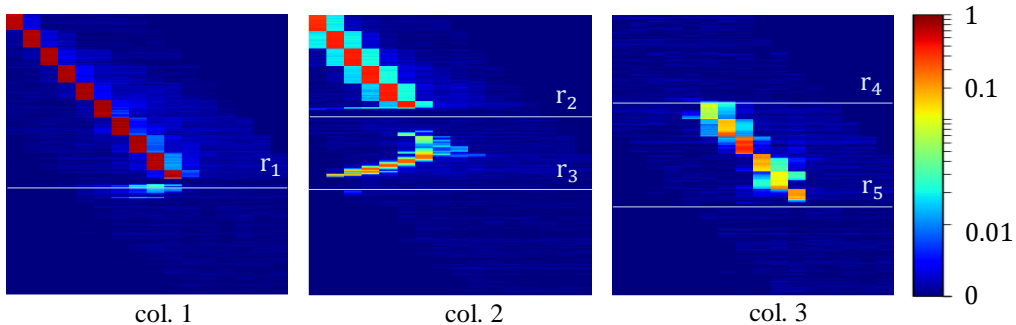


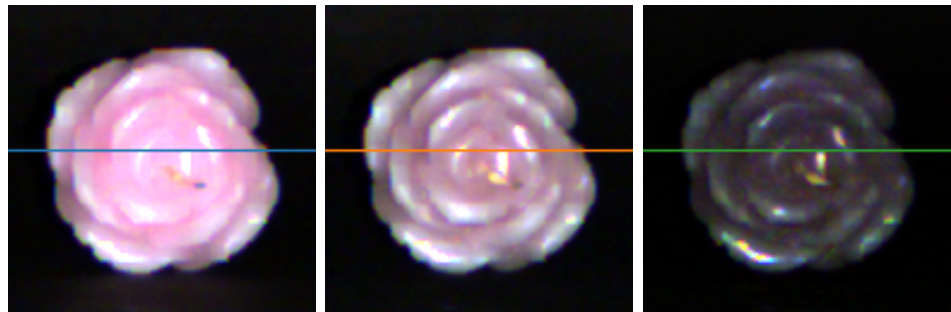
Figure 46. Light Transport Matrix. In contrast of most of light transport in col.1 is direct transport, there is short range light transport caused by refraction and subsurface scattering in col.2 and col.3.

in Figure 47(c) a tighter epipolar image than a regular epipolar image with exposure $t_e = 600\mu s$ shown in Figure 47(b). Note how the regular epipolar image cannot remove the subsurface scattering of the candle, but the sharpened epipolar image removes all these effects. Looking at the cross-section pixel values in Figure 47(d), the sharper epipolar image has more contrast amongst its rose petals. This sharpening has applications for when the system has a large exposure, and thus needs computation to generate a tighter epipolar image.

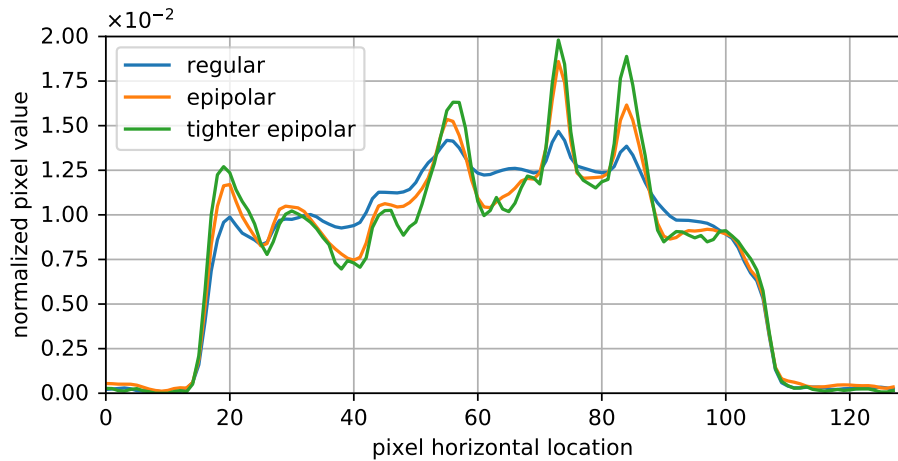
5.4.6 Epipolar direct/global separation

In this experiment, we show direct/global separation using plane-to-ray light transport. One of the disadvantages of epipolar imaging in this configuration is that it is difficult to separate epipolar indirect light from the image, and thus achieve true direct/global separation. To solve this, we thus apply the method from Nayar et al. [74] on the epipolar images alone. We used 128 shifting patterns of 24×24 pixel checkerboard for our implementation.

In Figure 48, we perform direct/global separation on a scene consisting of a wax bowl and disco ball. We note that the method from Nayar et al. fails on removing the specular interreflections of the disco ball as shown in Figure 48(b). Epipolar imaging thus improves upon Nayar et al. by removing these highlights in Figure 48(c). Combining the two methods results in an epipolar-direct image in Figure 48(d) and an epipolar-global image in Figure 48(e). Note that the epipolar-



(a) regular image (b) epipolar image (c) tighter epipolar (scaled $\times 8$ compared to (b))



(d) shading profile

Figure 47. Imaging a wax rose candle in epipolar mode (b) with an exposure of $600\mu s$ does not remove the subsurface scattering. Demultiplexing the image stack to recover 3D light transport, we synthesize a tighter epipolar image in (c) which preserves sharp features and highlights while removing the subsurface scattering from the epipolar image. In (d), we plot pixel values for a single scan line for comparison, note how the tighter epipolar image has larger contrast.

direct image is improved over each method alone, but still cannot completely remove all the specular interreflections on the epipolar plane. This is still an open problem for direct/global separation and warrants further study.

5.4.7 Visualization of vein

By acquiring an appropriate indirect plane-to-ray transport, the hidden structure can be visualized. In this experiment, we visualize the human vein under the skin. **Parameter setting** The vein is difficult to find in the regular image (Fig. 49(a)) since the diffuse reflection from the skin surface is usually dominant so that it hides the reflection from the vein. In order to remove the direct reflection, delay should be more than half of exposure, therefore, it should satisfy $t_d \leq \frac{1}{2}t_e$. The vein is most clearly visualized when only the reflection from the vein is captured. Fig. 49(b) shows an indirect image with large t_d . We can see the direct reflection from the skin surface is removed, however, the reflection from vein is also removed. With the delay t_d which is chosen carefully, the vein is clearly visualized as shown in Fig. 49(c). An appropriate delay depends on the distance to the arm, a depth of the vein, and a speed of raster-scan of the projector. Relationship between delay and visualization quality, and optimization of parameters require further study.

It is known that the vein is clearly visualized by near-infrared (NIR) imaging, and products called vein finder [75, 76] are commercially available. NIR light penetrates a skin well since reflection from the skin is weak, however, it is absorbed by haemoglobin in the blood. As a result, reflection from other tissue around a vein is stronger than the reflection from the vein, thus the vein is visualized. Since proposed method remove the reflection based on the light paths, it does not depend on the transmittance of the skin. It should be meaningful to compare these two methods to clarify their ability to visualize depending on colors and thickness of the skin for future study. Finally, it is noteworthy to mention that these two methods can be used at the same time if it produce a clearer image.

5.4.8 Appearance capture for graphics

Acquire light transport can be applied for graphics rendering. In this experiment, we acquire the plane-to-ray light transport of soap (Fig. 50(a)), that exhibit



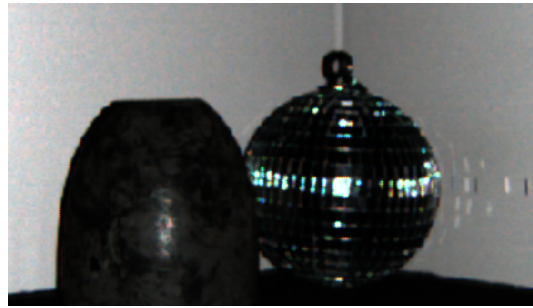
(a) Regular image



(b) Direct image using Nayar et al. [74] applied to (a)



(c) Epipolar image [69]



(d) Epipolar-direct image

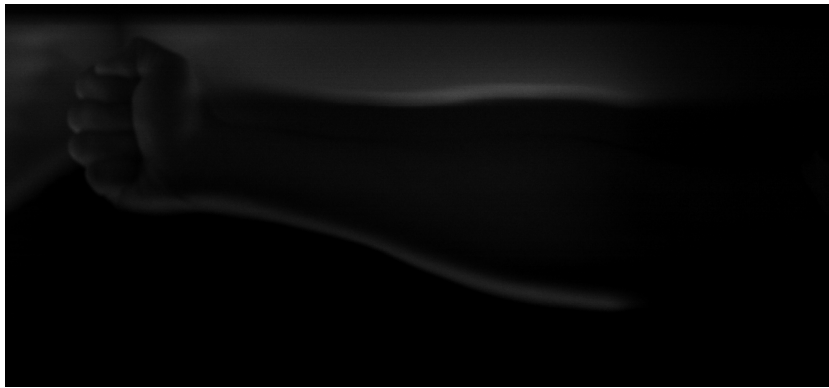


(e) Epipolar-global image (scaled x18 for visualization)

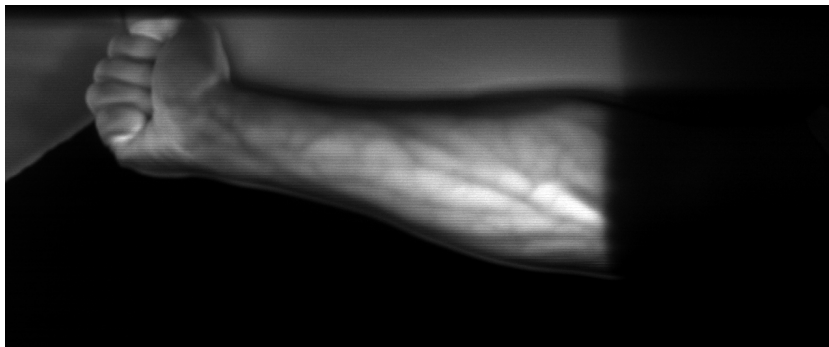
Figure 48. We show the results of two direct/global separation methods on our scene (a): Nayar et al. [74] in (b), and epipolar imaging [69] in (c). By combining the two methods, we are able to visualize (d) epipolar-direct only light, and (e) epipolar-global light. Notice how the specular interreflections are only removed in epipolar imaging, and the remaining subsurface scattering light in the epipolar image is separated by combining both algorithms.



(a) regular image



(b) far range indirect



(c) indirect with appropriate delay

Figure 49. Visualization of vein. In regular image (a), veins are hidden under the reflection on the skin. (b) Direct reflection is removed by using far range indirect, however, reflection from the vein is also removed. (c) Using appropriate delay, the reflection from vein is visualized.

spatially-varying subsurface scattering. We render the models with the effect of subsurface scattering, and without the effect for the comparison. Specular reflection is attached as a post process for better perception. We assume the effect of subsurface scattering depends only on the transport distance, and the effect can be approximated by the delay sweep profile.

The result of teapot and bunny are shown in Fig. 50(a), (c) (with subsurface effect), and (b), (d) (without effect) respectively. The object is lit with a point light at left top. We can see the light blooming due to the effect of subsurface scattering, which is significant in the right half of teapot, and ears of the bunny.

5.4.9 Material Recognition of Subsurface Scattering

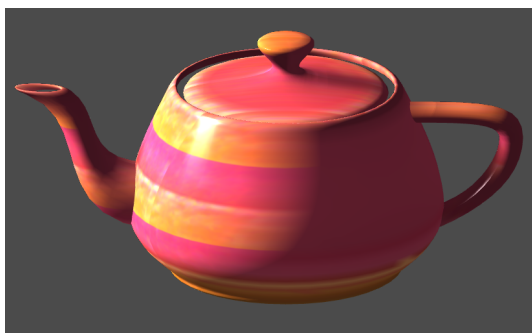
The use of delay and exposure can yield fundamental new information about light scattering in materials, particularly subsurface scattering. Previous researchers have used time-of-flight measurements to achieve a similar result [77, 73]. Consider the delay profile for a given material. We expect the maximum of this plot to be at $t_d = 0$. However, our intuition is that the more subsurface scattering present in the material, the more spread out the delay profile will be.

In Fig. 51(a), we tested this hypothesis and its usefulness for material recognition of subsurface scattering in common household items. We imaged hand soap, fat free, 2%, and whole milk, and toothpaste. All of these items were white in color, and difficult to identify with RGB information alone. We plotted their average delay profiles for a set of their pixels shown in Fig. 51(b). We normalized these delay profiles using the area under the curve to cancel out the effects of albedo.

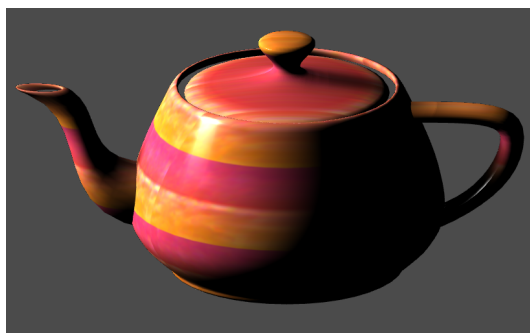
Using training and test images, we trained a support vector machine (SVM) with nonlinear kernel (radial Gaussian basis function) to get a per-pixel semantic segmentation of the materials (Fig. 51(c)) and a confusion matrix (Fig. 52). We achieved over 90% recognition for all the materials. We note that the only errors occurred for pixels near the edge of the container, where possibly the scattering profile changes for the materials due to the asymmetry of a boundary condition. This is an interesting avenue of future research to use delay profiles to better model or inverse render subsurface scattering. This application is not meant for robust instance-level material recognition, but highlights the usefulness of delay



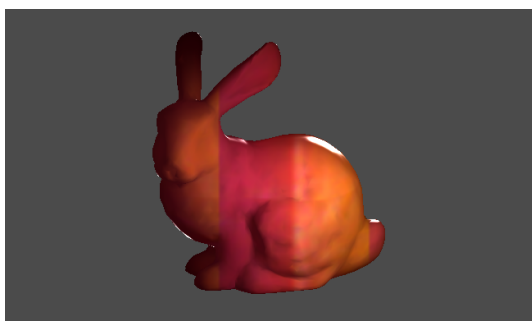
(a) Source material (soap)



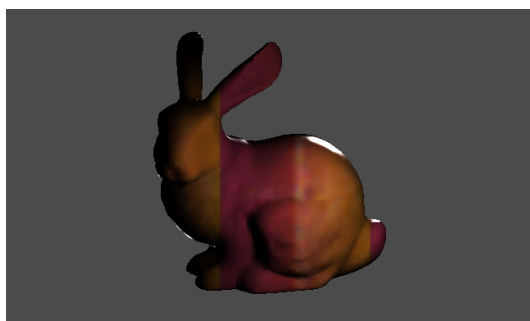
(b) Teapot with subsurface effect



(c) Teapot without subsurface effect



(d) Bunny with subsurface effect



(e) Bunny without subsurface effect

Figure 50. Appearance capture for graphics. We transfer source material (a) to teapot and bunny models. Directional light is cast from left side in teapot scene, and from top-right in bunny scene. By including subsurface effect (b), (d), the areas which are not directly illuminated became brighter compared to image rendered without the effect (c), (e).

profiles for understanding subsurface scattering in materials.

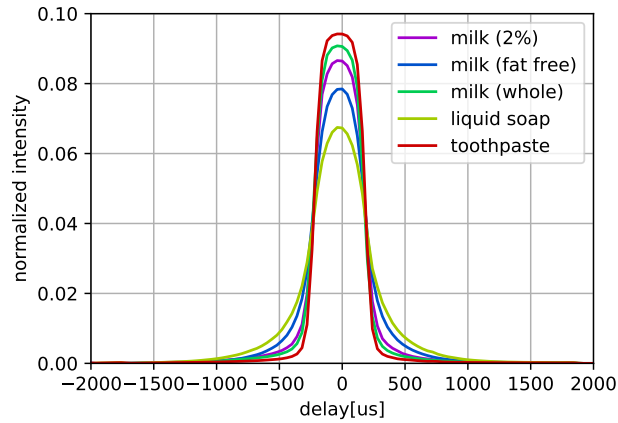
5.4.10 Acquired materials

Finally, we acquire the full light transport profile of several materials in Fig. 53. We use $l_w = 10\text{px}$, $l_d = 5\text{px}$ to $l_d = 995\text{px}$ at every 1px , $t_e = 170\mu\text{s}$, and $t_d = -340\mu\text{s}$ to $t_d = 340\mu\text{s}$ at every $17\mu\text{s}$. Each profile describes the transport to pixels shown in the appearance, from the relative illumination positions. Profiles have 41 columns and 41 rows that correspond to approximately $10\text{mm} \times 10\text{mm}$ in physical size. Profile values are normalized by its maximum after adjusting the white balance.

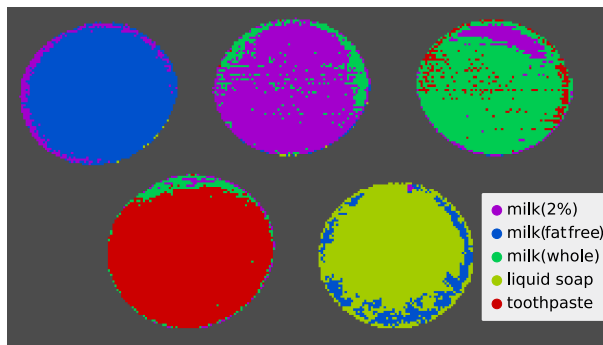
Let us take a look at the profile of materials shown in Fig. 53. (a) is the profile of a wooden ball that is considered to have Lambertian surface. The profile is isotropic and has small extent. (b) candle are the examples of subsurface scattering materials. It has a larger extent than the that of the wooden ball. (c) is a cube whose surface exhibit a diffuse reflection and little specular reflection. The profiles are similar to diffuse surface at (c1) and (c2), and at (c) we can see a effect of inter-reflection between floor. (d) is a fake apple that is made of Styrofoam and covered with the surface with texture. We can see the shape of the profiles are the same at (d1), (d2), and (d3), beside the colors are different. (e) sponge and (f) marble are the examples of heterogeneous materials. In the profile of sponge, the profiles of pink (d1) and red (d2) pixels have similar extent because the scattering property of the material are same, while the color are different from each other. In the profile of marble, the pixel (f1) has slightly wider extent compared to (f2) since the each composition has different scattering property. Finally, (g) is the example of inhomogeneous materials. A miniature of the Jeditte Cabbage is made of plastic whose color are gradually changing from green to white (left to right). At (g1) almost all the pixels are green and at (g3) all the pixels are white. The profile at (g2) is the mixture of the green and the white pixel since the incident light reached in both green and white surfaces contribute to the pixel (g2).



(a) Materials



(b) Delay profile



(c) Classification result

Figure 51. Material classification using plane-to-ray light transport. We hardly classify the materials from the color image (a). However, delay profiles are clearly different (b), therefore, they are classified at the most pixels (c).

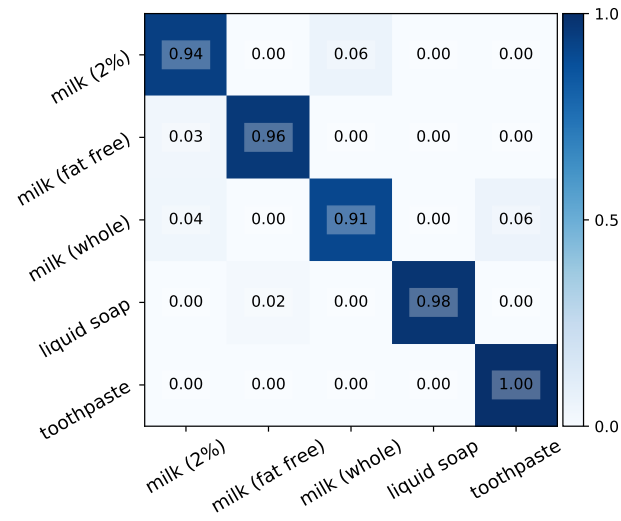


Figure 52. Confusion matrix (Non-linear SVM). We achieved over 90% recognition for all the materials.

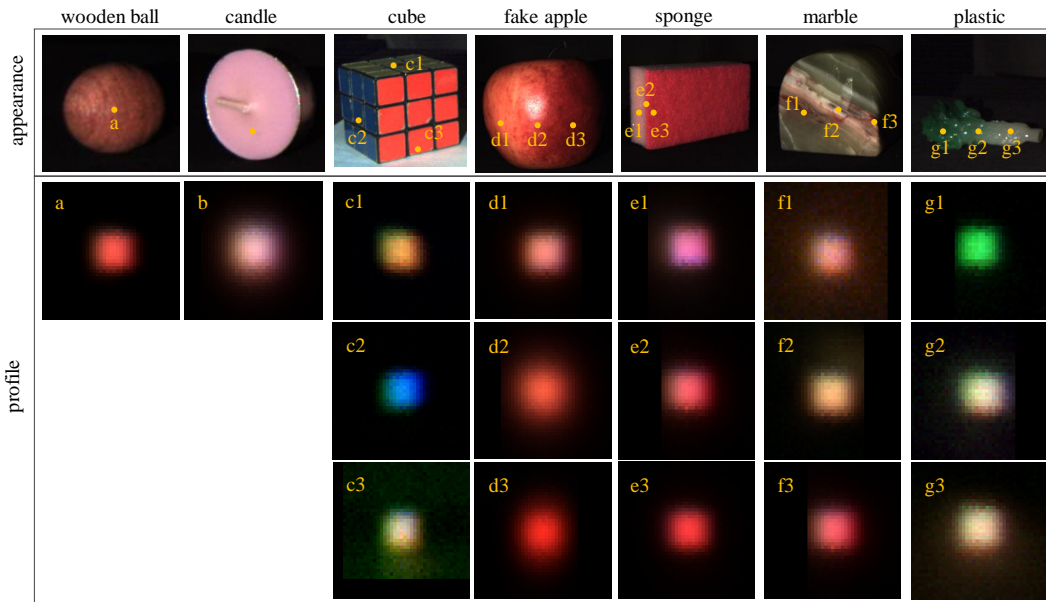


Figure 53. Appearance and profiles of various materials. Profiles shows difference due to light behavior such like diffuse reflections, or subsurface scattering, and spatial variation.

5.5 Conclusion

We have proposed a measurement method of 4D light transport using the synchronized projector camera system. In this method, we project a vertical line to control illumination along the horizontal axis, while delay and exposure are changed to control illumination along the vertical axis. We performed the illumination multiplexing to increase the amount of light for each measurement. We showed the reconstructed light transport via demultiplexing has better quality than simplex measurement.

One of the limitations is that we cannot increase exposure to accumulate more light. This could be a problem when the only little light returns from the scene.

Possible extension of this work is to find more efficient ways of illumination multiplexing. For example, a technique based on Hadamard codes [70, 78] may efficiently improve SNR.

6. Conclusions and Future work

6.1 Conclusions

In this thesis, we discussed about the light transport acquisition and the application of acquired light transport. Light transport is complicating process relating to the geometry of the scene and light behavior. The problem is how we acquire desired light transport in the presence of undesired light transport. To deal with this problem, we propose the selective path measurement. We specify paths by considering the geometry and the measurement setup, and selectively acquire the light transport along the path. Also proposal of analysis and application of light transport is our contribution. In Sec. 2, we have explained basic theory of light transport and representation of light transport. In Sec. 3, we have introduced related work to show our contributions.

We tackle two problem settings. In Sec. 4, we tackle an optical tomography of diffuse surface object that has a diffuse surface and a transparent body. To reconstruct the interior of the object, light paths are required to be specified. We have proposed the shortest path model to represent light path in diffuse surface object. We have proposed the acquisition of light transport along shortest path and the reconstruction algorithm. We have discussed about the observation rate, the optimal setup, and robustness to scattering. We have demonstrated that the interior of a real object is successfully reconstructed by our framework. In Sec. 5, we tackle light transport acquisition of projector camera system. The difficulty of this problem is that it requires a numerous number of sampling due to the resolutions of projector and camera. For the efficient acquisition of light transport, we have proposed acquisition according to transport distance using synchronized projector camera system. We have proposed plane-to-ray light transport that is closely related to the synchronized system. The plane-to-ray light transport is acquired efficiently by synchronizing the rolling-shutter of a camera to a fixed offset of the raster-scan of projector in vertical direction. The acquisition have been extended to the acquisition of the full light transport by projecting a vertical line to acquire light transport in horizontal direction. We have shown visualization and application using the acquired light transport. We have shown analysis of light behavior, relighting, illumination multiplexing, direct/global separation, vi-

sualization of vein, material classification, and appearance capture for computer graphics.

Our proposal of light transport acquisition via light path measurement allows us to visualize the interior of the object, visualize and analyze the scene in the presence of complicated light transport. However, there are some limitations in our methods. For the problem of optical tomography, we have assumed the diffuse surface object. From the discussion, the effect of scattering and inter-reflection in the object degrades the reconstruction. Also, a shape of the object is limited to convex. For the acquisition in projector-camera system, the projector and camera are in rectified stereo setup. It results in the difficulty to acquire transport with angular variations.

6.2 Future work

Finally, we would like to show future direction of our work.

We acquire the light transport by actual measurement. One possible way to reduce the cost of the measurement is to measure only part of the light transport and to estimate remaining part. For example, compressive sensing[79] can be applied for the case the data is assumed sparse. Also, machine learning techniques can be applied for designing optimal measurement like in [22, 80].

Another direction is to explore the other dimensions of the plenoptic function. We have only considered the location and the angular of the light. A wavelength is interesting domain since the spectral response is related to the chemical substance and fluorescence that could found practical applications in the medical inspection or the food production. A time domain is also interesting since the temporal response is a great cue of scene understanding as some recent work reveal.

Like we utilized synchronized projector camera in Sec. 5, light transport acquisition is closely related to hardware. There are lot of conventional and emerging hardware to combine, such like MEMS mirror, multi-bucket sensor [81], and angle sensitive pixel [82, 83]. The utilization of such hardware may allow us to novel acquisition of light transport.

We believe our concept of selective path measurement is a general framework that extends the possibility of scene analysis and further applications.

Acknowledgements

This work was completed in Graduate School of Information Science, Nara Institute of Science and Technology. This has not been possible without all the support of many people.

First of all, I would like to express my appreciation to my advisor Professor Yasuhiro Mukaigawa for his support and advice. He made me find out the fun of computer vision with his passionate words. It was a precious experience to share the first five years of the new laboratory as one of the first students. I would like to sincerely thank to Professor Yoshinobu Sato, who kindly undertook the committee member of this dissertation for his constructive comments and suggestions. I am deeply grateful to Professor Takuya Funatomi for his teaching with a lot of patience and for inspiring me through a lot of discussions. I would like to thank Professor Hiroyuki Kubo for giving me advises not only for the research, but also for many situations during my Ph.D course. I also would like to thank Professor Kenichiro Tanaka, who keep giving me kind advice as a Ph.D student and as an assistant professor.

I am grateful to Professor Srinivasa Narasimhan at Carnegie Mellon University, who kindly accept my visit over seven months and continuous collaboration after the stay. Chapter 5 is based on the study during my stay at his laboratory. I would like to thank all the members of the optical media interface laboratory for sharing the time in the laboratory, for their work and their leisure. I would like to appreciate secretaries Ms. Toshie Nobori and Ms. Yumi Irie for the great support in the accounting tasks. It helps me concentrate the research activity.

Finally, I would like to thank my family for their understanding, supports and encourages.

References

- [1] P. Will and K. Pennington, “Grid coding: A preprocessing technique for robot and machine vision,” *Artificial Intelligence*, vol. 2, no. 3, pp. 319–329, 1971.
- [2] M. Minou, T. Kanade, and T. Sakai, “A Method of Time-Coded Parallel Planes of Light for Depth Measurement,” *Trans. Institute of Electronics and Communication Engineers of Japan*, vol. E64, no. 8, pp. 521–528, 1981.
- [3] R. J. Woodham, “Photometric method for determining surface orientation from multiple images,” *Optical Engineering*, vol. 19, no. 1, pp. 139–144, 1980.
- [4] B. K. P. Horn, “Obtaining shape from shading information,” in *Shape from Shading*, 1989, pp. 123–171.
- [5] W. R. Alpers, D. B. Ross, and C. L. Rufenach, “On the detectability of ocean surface waves by real and synthetic aperture radar,” *Journal of Geophysical Research*, vol. 86, no. C7, pp. 6481–6498, 1981.
- [6] M. Gupta, A. Agrawal, A. Veeraraghavan, and S. G. Narasimhan, “Structured light 3D scanning in the presence of global illumination,” in *Proceedings of the IEEE Conference on Computer Vision and Pattern Recognition (CVPR)*, 2011, pp. 713–720.
- [7] T. Chen, H. P. A. Lensch, C. Fuchs, and H. Seidel, “Polarization and Phase-Shifting for 3D Scanning of Translucent Objects,” in *Proceedings of the IEEE Conference on Computer Vision and Pattern Recognition (CVPR)*, 2007, pp. 1–8.
- [8] M. Gupta, S. G. Narasimhan, and Y. Y. Schechner, “On controlling light transport in poor visibility environments,” in *Proceedings of the IEEE Conference on Computer Vision and Pattern Recognition (CVPR)*, 2008, pp. 1–8.
- [9] M. P. Rowe, E. N. Pugh, J. S. Tyo, and N. Engheta, “Polarization-difference imaging: a biologically inspired technique for observation through scattering media,” *Optics Letters*, vol. 20, no. 6, pp. 608–610, 1995.

- [10] E. H. Adelson and J. R. Bergen, “The plenoptic function and the elements of early vision,” in *Computational Models of Visual Processing*. MIT Press, 1991, pp. 3–20.
- [11] J. Lengyel, “The Convergence of Graphics and Vision,” *Computer*, vol. 31, no. 7, pp. 46–53, 1998.
- [12] C. Zhang and T. Chen, “A survey on image-based rendering—representation, sampling and compression,” *Signal Processing: Image Communication*, vol. 19, no. 1, pp. 1–28, 2004.
- [13] J.-X. Chai, X. Tong, S.-C. Chan, and H.-Y. Shum, “Plenoptic Sampling,” in *Proceedings of the 27th Annual Conference on Computer Graphics and Interactive Techniques*, 2000, pp. 307–318.
- [14] M. Levoy and P. Hanrahan, “Light Field Rendering,” in *Proceedings of the 23rd Annual Conference on Computer Graphics and Interactive Techniques*, 1996, pp. 31–42.
- [15] S. J. Gortler, R. Grzeszczuk, R. Szeliski, and M. F. Cohen, “The Lumi-graph,” in *Proceedings of the 23rd Annual Conference on Computer Graphics and Interactive Techniques*, 1996, pp. 43–54.
- [16] M. Levoy, B. Chen, V. Vaish, M. Horowitz, I. McDowall, and M. Bolas, “Synthetic Aperture Confocal Imaging,” *ACM Transactions on Graphics (ToG)*, vol. 23, no. 3, pp. 825–834, 2004.
- [17] R. Ng, “Fourier Slice Photography,” *ACM Transactions on Graphics (ToG)*, vol. 24, no. 3, pp. 735–744, 2005.
- [18] R. Ng, M. Levoy, M. Brédif, G. Duval, M. Horowitz, and P. Hanrahan, “Light Field Photography with a Hand-Held Plenoptic Camera,” *Stanford University Computer Science Tech Report*, vol. 2, 2005.
- [19] F. E. Nicodemus, J. C. Richmond, J. J. Hsia, I. W. Ginsberg, and T. Limperis, “Geometrical considerations and nomenclature for reflectance,” in *Radiometry*, pp. 94–145.

- [20] K. J. Dana, B. van Ginneken, S. K. Nayar, and J. J. Koenderink, “Reflectance and Texture of Real-world Surfaces,” *ACM Transactions on Graphics (ToG)*, vol. 18, no. 1, pp. 1–34, 1999.
- [21] J. Lawrence, A. Ben-Artzi, C. DeCoro, W. Matusik, H. Pfister, R. Ramamoorthi, and S. Rusinkiewicz, “Inverse Shade Trees for Non-parametric Material Representation and Editing,” *ACM Transactions on Graphics (ToG)*, vol. 25, no. 3, pp. 735–745, 2006.
- [22] K. Kang, Z. Chen, J. Wang, K. Zhou, and H. Wu, “Efficient Reflectance Capture Using an Autoencoder,” *ACM Transactions on Graphics (ToG)*, vol. 37, no. 4, pp. 1–10, 2018.
- [23] M. Ben-Ezra, J. Wang, B. Wilburn, X. Li, and L. Ma, “An LED-only BRDF measurement device,” in *Proceedings of the IEEE Conference on Computer Vision and Pattern Recognition (CVPR)*, 2008, pp. 1–8.
- [24] M. Aittala, T. Weyrich, and J. Lehtinen, “Practical SVBRDF capture in the frequency domain,” *ACM Transactions on Graphics (ToG)*, vol. 32, no. 4, pp. 1–12, 2013.
- [25] P. Debevec, T. Hawkins, C. Tchou, H.-P. Duiker, W. Sarokin, and M. Sagar, “Acquiring the Reflectance Field of a Human Face,” in *Proceedings of the 27th Annual Conference on Computer Graphics and Interactive Techniques*, 2000, pp. 145–156.
- [26] V. Masselus, P. Peers, P. Dutré, and Y. D. Willems, “Relighting with 4D Incident Light Fields,” *ACM Transactions on Graphics (ToG)*, vol. 22, no. 3, pp. 613–620, 2003.
- [27] D. N. Wood, D. I. Azuma, K. Aldinger, B. Curless, T. Duchamp, D. H. Salesin, and W. Stuetzle, “Surface Light Fields for 3D Photography,” in *Proceedings of the 27th Annual Conference on Computer Graphics and Interactive Techniques*, 2000, pp. 287–296.
- [28] J. H. Lambert, “Photometria sive de mensura de gratibus luminis,” *Eberhard Klett in Eberhard Klett*, 1760.

- [29] B. T. Phong, “Illumination for computer generated pictures,” *Communications of the ACM*, vol. 18, no. 6, pp. 311–317, 1975.
- [30] K. E. Torrance and E. M. Sparrow, “Theory for off-specular reflection from roughened surfaces,” in *Radiometry*, 1992, pp. 32–41.
- [31] P. Peers, K. vom Berge, W. Matusik, R. Ramamoorthi, J. Lawrence, S. Rusinkiewicz, and P. Dutré, “A Compact Factored Representation of Heterogeneous Subsurface Scattering,” in *Proceedings of ACM SIGGRAPH*, 2006, pp. 746–753.
- [32] W. Matusik, H. Pfister, M. Brand, and L. McMillan, “Efficient isotropic brdf measurement,” in *Proceedings of the 14th Eurographics Workshop on Rendering*. Eurographics Association, 2003, pp. 241–247.
- [33] J. Filip, R. Vavra, M. Haindl, P. Zid, M. Krupika, and V. Havran, “BRDF Slices: Accurate Adaptive Anisotropic Appearance Acquisition,” in *Proceedings of the IEEE Conference on Computer Vision and Pattern Recognition (CVPR)*, 2013, pp. 1468–1473.
- [34] C. Donner, T. Weyrich, E. d’Eon, R. Ramamoorthi, and S. Rusinkiewicz, “A Layered, Heterogeneous Reflectance Model for Acquiring and Rendering Human Skin,” in *Proceedings of ACM SIGGRAPH Asia*, 2008, pp. 1–12.
- [35] S. Premože, M. Ashikhmin, J. Tessendorf, R. Ramamoorthi, and S. Nayar, “Practical Rendering of Multiple Scattering Effects in Participating Media,” in *Proceedings of the Fifteenth Eurographics Conference on Rendering Techniques*, 2004, pp. 363–374.
- [36] S. G. Narasimhan, M. Gupta, C. Donner, R. Ramamoorthi, S. K. Nayar, and H. W. Jensen, “Acquiring Scattering Properties of Participating Media by Dilution,” *ACM Transactions on Graphics (ToG)*, vol. 25, no. 3, pp. 1003–1012, 2006.
- [37] C. Haisch, “Optical Tomography,” *Annual Review of Analytical Chemistry*, vol. 5, no. 1, pp. 57–77, 2012.

- [38] J. Sharpe, “Optical projection tomography,” *Annu. Rev. Biomed. Eng.*, vol. 6, pp. 209–228, 2004.
- [39] F. Natterer, *The Mathematics of Computerized Tomography*. Society for Industrial and Applied Mathematics, 2001.
- [40] L. Florescu, J. C. Schotland, and V. A. Markel, “Single-scattering optical tomography,” *Physical Review E*, vol. 79, no. 3, p. 036607, 2009.
- [41] B. Yuan, T. Tamaki, T. Kushida, Y. Mukaigawa, H. Kubo, B. Raytchev, and K. Kaneda, “Optical tomography with discretized path integral,” *Journal of Medical Imaging*, vol. 2, pp. 2–16, 2015.
- [42] Y. Ishii, T. Arai, Y. Mukaigawa, J. Tagawa, and Y. Yagi, “Scattering tomography by monte carlo voting,” in *IAPR International Conference on Machine Vision Applications*, no. 1, 2013, pp. 1–5.
- [43] R. Akashi, H. Nagahara, Y. Mukaigawa, and R. Taniguchi, “Scattering tomography using ellipsoidal mirror,” in *2015 21st Korea-Japan Joint Workshop on Frontiers of Computer Vision (FCV)*, 2015, pp. 1–5.
- [44] V. Ntziachristos, A. Yodh, M. Schnall, and B. Chance, “Concurrent mri and diffuse optical tomography of breast after indocyanine green enhancement,” *Proceedings of the National Academy of Sciences*, vol. 97, no. 6, pp. 2767–2772, 2000.
- [45] J. C. Hebden, A. Gibson, R. M. Yusof, N. Everdell, E. M. Hillman, D. T. Delpy, S. R. Arridge, T. Austin, J. H. Meek, and J. S. Wyatt, “Three-dimensional optical tomography of the premature infant brain,” *Physics in medicine and biology*, vol. 47, no. 23, p. 4155, 2002.
- [46] J. P. Culver, A. M. Siegel, J. J. Stott, and D. A. Boas, “Volumetric diffuse optical tomography of brain activity,” *Optics letters*, vol. 28, no. 21, pp. 2061–2063, 2003.
- [47] P. Sen, B. Chen, G. Garg, S. R. Marschner, M. Horowitz, M. Levoy, and H. P. A. Lensch, “Dual photography,” *ACM Transactions on Graphics (ToG)*, vol. 24, no. 3, pp. 745–755, 2005.

- [48] P. Sen and S. Darabi, “Compressive Dual Photography,” *Computer Graphics Forum*, vol. 28, pp. 609–618, 2009.
- [49] P. Peers, D. K. Mahajan, B. Lamond, A. Ghosh, W. Matusik, R. Ramamoorthi, and P. Debevec, “Compressive Light Transport Sensing,” *ACM Transactions on Graphics (ToG)*, vol. 28, no. 1, pp. 1–18, 2009.
- [50] G. Garg, E.-V. Talvala, M. Levoy, and H. P. Lensch, “Symmetric Photography: Exploiting Data-sparseness in Reflectance Fields,” in *Proceedings of the 17th Eurographics Conference on Rendering Techniques*, 2006, pp. 251–262.
- [51] J. Wang, Y. Dong, X. Tong, Z. Lin, and B. Guo, “Kernel Nyström Method for Light Transport,” *ACM Transactions on Graphics (ToG)*, vol. 28, no. 3, pp. 1–10, 2009.
- [52] M. O’Toole and K. N. Kutulakos, “Optical Computing for Fast Light Transport Analysis,” *ACM Transactions on Graphics (ToG)*, vol. 29, no. 6, pp. 1–12, 2010.
- [53] A. Laurentini, “The visual hull concept for silhouette-based image understanding,” *IEEE Transactions on Pattern Analysis and Machine Intelligence (TPAMI)*, vol. 16, no. 2, pp. 150–162, 1994.
- [54] T. Iwaguchi, T. Funatomi, H. Kubo, and Y. Mukaigawa, “Light path alignment for computed tomography of scattering material,” *IPSS Transactions on Computer Vision and Applications*, vol. 8, no. 1, p. 2, 2016.
- [55] D. L. Parker, “Optimal short scan convolution reconstruction for fan beam CT,” *Medical Physics*, vol. 9, no. 2, pp. 254–257, 1982.
- [56] G. L. Zeng, “The fan-beam short-scan FBP algorithm is not exact,” *Physics in Medicine and Biology*, vol. 60, no. 8, pp. 131–139, 2015.
- [57] R. Gordon, R. Bender, and G. T. Herman, “Algebraic reconstruction techniques (art) for three-dimensional electron microscopy and x-ray photography,” *Journal of theoretical Biology*, vol. 29, no. 3, pp. 471–481, 1970.

- [58] A. H. Andersen and A. C. Kak, “Simultaneous algebraic reconstruction technique (sart): a superior implementation of the art algorithm,” *Ultrasonic imaging*, vol. 6, no. 1, pp. 81–94, 1984.
- [59] B. P. Medoff, W. R. Brody, M. Nassi, and A. Macovski, “Iterative convolution backprojection algorithms for image reconstruction from limited data,” *Journal of the Optical Society of America*, vol. 73, no. 11, pp. 1493–1500, 1984.
- [60] A. H. Delaney and Y. Bresler, “A fast and accurate Fourier algorithm for iterative parallel-beam tomography,” *IEEE Transactions on Image Processing*, vol. 5, no. 5, pp. 740–753, 1996.
- [61] F. Noo, R. Clackdoyle, and J. Pack, “A two-step Hilbert transform method for 2D image reconstruction,” *Physics in Medicine and Biology*, vol. 49, no. 17, pp. 3903–3923, 2004.
- [62] M. Defrise, F. Noo, R. Clackdoyle, and H. Kudo, “Truncated hilbert transform and image reconstruction from limited tomographic data,” *Inverse Problems*, vol. 22, no. 3, p. 1037, 2006.
- [63] S. J. LaRoque, E. Y. Sidky, and X. Pan, “Accurate image reconstruction from few-view and limited-angle data in diffraction tomography,” *Journal of the Optical Society of America*, vol. 25, no. 7, pp. 1772–1782, 2008.
- [64] G.-H. Chen, J. Tang, and S. Leng, “Prior image constrained compressed sensing (PICCS): A method to accurately reconstruct dynamic CT images from highly undersampled projection data sets,” *Medical Physics*, vol. 35, no. 2, pp. 660–663, 2008.
- [65] H. W. Jensen and P. H. Christensen, “Efficient simulation of light transport in scenes with participating media using photon maps,” in *Proceedings of the 25th annual conference on Computer graphics and interactive techniques*, 1998, pp. 311–320.
- [66] C. Fuchs, M. Heinz, M. Levoy, H.-P. Seidel, and H. P. Lensch, “Combining Confocal Imaging and Descattering,” in *Proceedings of the Nineteenth Eurographics Conference on Rendering*, 2008, pp. 1245–1253.

- [67] “Recovering Inner Slices of Layered Translucent Objects by Multi-Frequency Illumination,” *IEEE Transactions on Pattern Analysis and Machine Intelligence (TPAMI)*, vol. 39, no. 4, pp. 746–757, 2017.
- [68] D. Reddy, R. Ramamoorthi, and B. Curless, “Frequency-space Decomposition and Acquisition of Light Transport Under Spatially Varying Illumination,” in *Proceedings of the European Conference on Computer Vision (ECCV)*, 2012, pp. 596–610.
- [69] M. O’Toole, S. Achar, S. G. Narasimhan, and K. N. Kutulakos, “Homogeneous Codes for Energy-efficient Illumination and Imaging,” *ACM Transactions on Graphics (ToG)*, vol. 34, no. 4, pp. 1–13, 2015.
- [70] Y. Y. Schechner, S. K. Nayar, and P. N. Belhumeur, “Multiplexing for Optimal Lighting,” *IEEE Transactions on Pattern Analysis and Machine Intelligence (TPAMI)*, vol. 29, no. 8, pp. 1339–1354, 2007.
- [71] S. Diamond and S. Boyd, “Cvxpy: A python-embedded modeling language for convex optimization,” *The Journal of Machine Learning Research*, vol. 17, no. 1, pp. 2909–2913, 2016.
- [72] M. O’Toole, J. Mather, and K. N. Kutulakos, “3d shape and indirect appearance by structured light transport,” in *Proceedings of the IEEE Conference on Computer Vision and Pattern Recognition (CVPR)*, 2014, pp. 3246–3253.
- [73] D. Wu, A. Velten, M. O’toole, B. Masia, A. Agrawal, Q. Dai, and R. Raskar, “Decomposing global light transport using time of flight imaging,” *International Journal of Computer Vision*, vol. 107, no. 2, pp. 123–138, 2014.
- [74] S. K. Nayar, G. Krishnan, M. D. Grossberg, and R. Raskar, “Fast Separation of Direct and Global Components of a Scene Using High Frequency Illumination,” *ACM Transactions on Graphics (ToG)*, vol. 25, no. 3, pp. 935–944, 2006.
- [75] “IV-EYE,” <http://novarix.com/iv-eye/>, accessed 2019-01-10.
- [76] “AccuVein,” <https://www.accuvein.com/>, accessed 2019-01-10.

- [77] S. Su, F. Heide, R. Swanson, J. Klein, C. Callenberg, M. Hullin, and W. Heidrich, “Material classification using raw time-of-flight measurements,” in *Proceedings of the IEEE Conference on Computer Vision and Pattern Recognition (CVPR)*, 2016, pp. 3503–3511.
- [78] N. Ratner and Y. Y. Schechner, “Illumination multiplexing within fundamental limits,” in *Proceedings of the IEEE Conference on Computer Vision and Pattern Recognition (CVPR)*, 2007, pp. 1–8.
- [79] R. G. Baraniuk, “Compressive Sensing [Lecture Notes],” *IEEE Signal Processing Magazine*, vol. 24, no. 4, pp. 118–121, 2007.
- [80] P. Mirdehghan, W. Chen, and K. N. Kutulakos, “Optimal Structured Light à La Carte,” in *Proceedings of the IEEE Conference on Computer Vision and Pattern Recognition (CVPR)*, 2018, pp. 6248–6257.
- [81] G. Wan, X. Li, G. Agranov, M. Levoy, and M. Horowitz, “CMOS Image Sensors With Multi-Bucket Pixels for Computational Photography,” *IEEE Journal of Solid-State Circuits*, vol. 47, no. 4, pp. 1031–1042, 2012.
- [82] M. Hirsch, S. Sivaramakrishnan, S. Jayasuriya, A. Wang, A. Molnar, R. Raskar, and G. Wetzstein, “A switchable light field camera architecture with Angle Sensitive Pixels and dictionary-based sparse coding,” in *Proceedings of the International Conference on Computational Photography (ICCP)*, 2014, pp. 1–10.
- [83] A. Wang, P. Gill, and A. Molnar, “Angle sensitive pixels in CMOS for lensless 3D imaging,” in *IEEE Custom Integrated Circuits Conference*, 2009, pp. 371–374.

List of Publications

Journal

1. T. Iwaguchi, T. Funatomi, T. Aoto, H. Kubo, Y. Mukaigawa, “Optical Tomography based on Shortest-path Model for Diffuse Surface Object”, *IPSJ Transactions on Computer Vision and Applications*, vol. 10, no. 1, 15, Nov. 2018.
2. T. Iwaguchi, T. Funatomi, H. Kubo, Y. Mukaigawa, “Light Path Alignment for Computed Tomography of Scattering Material”, *IPSJ Transactions on Computer Vision and Applications*, vol. 8, no. 1, 2, Dec. 2016.

International Conference (Reviewed)

1. T. Iwaguchi, H. Kubo, T. Funatomi, Y. Mukaigawa, S. Narasimhan, “Acquiring Short Range 4D Light Transport with Synchronized Projector Camera System”, in *Proceedings of ACM Symposium on Virtual Reality Software and Technology (VRST2018)*, no. 67, Dec. 2018.
2. H. Kubo, S. Jayasuriya, T. Iwaguchi, T. Funatomi, Y. Mukaigawa, S. Narasimhan, “Acquiring and Characterizing Plane-to-Ray Indirect Light Transport”, in *Proceedings of the International Conference on Computational Photography (ICCP)*, pp. 1–10, Jan. 2018.
3. X. Zeng, T. Iwaguchi, H. Kubo, T. Funatomi, Y. Mukaigawa, “Estimating Parameters of Subsurface Scattering using Directional Dipole Model”, in *Proceedings of NICOGRAPH International 2017*, pp. 41–48, Jun. 2017.

International Conference (Not reviewed)

1. H. Kubo, S. Jayasuriya, T. Iwaguchi, T. Funatomi, Y. Mukaigawa, S. G. Narasimhan, “Parametric Light Transport Acquisition and its Application to Medical Imaging”, 2nd International Symposium of the Research Project on Global Research Network for Healthy Society based on Collaboration Between Media Informatics and Sports Science, Feb. 2018.

2. X. Zeng, T. Iwaguchi, H. Kubo, T. Funatomi, Y. Mukaigawa, “Evaluating Inverse Rendering of Subsurface Scattering using Translucent Spherical Object”, 情処研報 CGVI 166-3, Mar. 2017.
3. H. Kubo, S. Jayasuriya, T. Iwaguchi, T. Funatomi, Y. Mukaigawa, S. G. Narasimhan, “Parametric Light Transport Acquisition and its Application to Medical Imaging”, 2nd International Symposium of the Research Project on Global Research Network for Healthy Society based on Collaboration Between Media Informatics and Sports Science, Feb. 2018.
4. T. Iwaguchi, “Measuring Sugar Content Distribution in Fruits by Spectral Analysis”, China-Japan Student Workshop 2015, Sep. 2015.

Domestic Conference (Reviewed)

1. T. Iwaguchi, T. Funatomi, H. Kubo, Y. Mukaigawa, “Light Path Alignment for Computed Tomography of Scattering Material”, 画像の認識・理解シンポジウム (MIRU2016), Aug. 2016.
2. 久保尋之, S. Jayasuriya, 岩口堯史, 船富卓哉, 向川康博, S. Narasimhan, “エピポーラ幾何に基づく Plane-to-Ray ライトトランスポートの計測と解析”, Visual Computing (VC2018), Jun. 2018.

Domestic Conference (Not reviewed)

1. X. Zeng, T. Iwaguchi, H. Kubo, T. Funatomi, Y. Mukaigawa, “Evaluating Inverse Rendering of Subsurface Scattering using Translucent Spherical Object”, 情処研報 CGVI 166-3, Mar. 2017.
2. 岩口堯史, 久保尋之, 船富卓哉, 向川康博, “CT と 2 波長特徴を用いた果実内の糖度分布推定”, 画像の認識・理解シンポジウム (MIRU2015), SS3-32, Jul. 2015.
3. 岩口堯史, 久保尋之, 向川康博, “2 波長から計算される特徴量の逆投影による果実内糖度分布推定”, 情処研報 CVIM 197-28, May 2015.

4. 三原基, 岩口堯史, 田中賢一郎, 久保尋之, 長原一, 向川康博, “光線空間を用いた不要物体除去リフォーカシング画像の生成”, 情処研報 CVIM 195-52, Jan. 2015.
5. 三原基, 浅田繁伸, 石原葵, 岩口堯史, 岡本貴典, 田中賢一郎, 久保尋之, 向川康博, “光線空間を用いた画素毎に独立したリフォーカシング”, 電気関係学会関西連合大会, Nov. 2014.

Award

1. Best Poster Award, Takafumi Iwaguchi, Hiroyuki Kubo, Takuya Funatomi, Yasuhiro Mukaigawa, Srinivasa Narasimhan, ”Acquiring Short Range 4D Light Transport with Synchronized Projector Camera System”, Proc. ACM Symposium on Virtual Reality Software and Technology (VRST) 2018, Dec. 2018.
2. Cyber Agent Award (Sponsor Award), Takafumi Iwaguchi, Hiroyuki Kubo, Takuya Funatomi, Yasuhiro Mukaigawa, Srinivasa Narasimhan, ”Acquiring Short Range 4D Light Transport with Synchronized Projector Camera System”, Proc. ACM Symposium on Virtual Reality Software and Technology (VRST), Dec. 2018.
3. MIRU 学生優秀賞, Takafumi Iwaguchi, Takuya Funatomi, Hiroyuki Kubo, Yasuhiro Mukaigawa, “Light Path Alignment for Computed Tomography of Scattering Material”, 第19回画像の認識・理解シンポジウム (MIRU2016), Aug. 2016.
4. 若手最優秀賞, 青砥隆仁, 井手口裕太, 岩口堯史, 岡本翠, 野沢綸佐, 藤田秀, 余錦澤, 第18回画像の認識・理解シンポジウム (MIRU2015) 若手の会, Jul. 2015.
5. MIRU デモ発表賞, 久保尋之, S. Jayasuriya, 岩口堯史, 船富卓哉, 向川康博, S. Narasimhan, “Plane-to-Ray ライトトランスポートの計測に基づく半透明物体内部のリアルタイムイメージング”, 画像の認識・理解シンポジウム (MIRU2018), Aug. 2018.

6. 優秀研究発表賞, 久保尋之, S. Jayasuriya, 岩口堯史, 船富卓哉, 向川康博, S. Narasimhan, “エピポーラ幾何に基づく Plane-to-Ray ライトトランスポートの計測と解析”, 情報処理学会 CGVI 研究会, Visual Computing シンポジウム 2018, Jun. 2018.
7. 最優秀賞, 三原基, 浅田繁伸, 石原葵, 岩口堯史, 岡本貴典, 田中賢一郎, 「写ラナイんです (余計なモノが)」, NAIST CICP (Creative and International Competitiveness Project) 2014, Mar. 2015.